OFFICE OF NAVAL RESEARCH

GRANT or CONTRACT: N00014-91J-1201

R&T CODE: 4133032
Richard Carlin

TECHNICAL REPORT NO. 19

"Nanomaterials in Electrochemistry"

by Charles R. Martin

Prepared for Publication

in

Electroanalytical Chemistry

Colorado State University
Department of Chemistry
Fort Collins, CO 80523-1872

July 1, 1998

19980720 162

Reproduction in whole, or in part, is permitted for any purpose of the United States Government.

This document has been approved for public release and sale; its distribution is unlimited.

REPORT DOCUMENTATION PAGE

2. July 1, 1998

3. Interim report

4. "Nanomaterials in Electrochemistry"

5. GRANT: N00014-91J-1201, R&T CODE: 4133032

6. Charles R. Martin

7. Charles R. Martin, Department of Chemistry, Colorado State University, Fort Collins, CO 80523-1872

8. TECHNICAL REPORT NO. 19

9. Office of Naval Research, Chemistry Division, 800 North Quincy Street, Arlington, VA 22217-5660

11. To be published in *Electroanalytical Chemistry*

12. Reproduction in whole or in part is permitted for any purpose of the United States Government. This document has been approved for public release and sale; its distribution is unlimited.

13. Abstract: Nanomaterials and electrochemistry have a long shared history, for example, the use of finely dispersed Pt particles as catalysts in fuel cell electrodes. This chapter, however, deals specifically with applications of template-synthesized nanomaterials in electrochemistry. We begin with an overview of template materials. Three possible electrochemical applications of such materials are then discussed. The first entails use of the template method for preparing ensembles of nanoscopic electrodes. The second application concerns the development of a new type of ion-permselective membrane - the metal nanotubule membrane. These membranes can be viewed as universal ion exchangers as they can be electrochemically switched between cation permselective, anion permselective and non-permselective states. The transport properties of metal nanotubule membranes can also be made selective on the basis of either size or chemistry of the molecule to be transported.; possible applications of these membranes in chemical separations are discussed. The final application reviewed here entails the use of the template method to prepare monodisperse nanoparticles of Li^+-intercalation materials for possible use as electrodes in Li-ion batteries.

14. Subject terms: Nanomaterials, electrochemistry, nanoelectrodes.

17. 18. 19. Unclassified

Nanomaterials in Electrochemistry

Charles R. Martin
Department of Chemistry
Colorado State University
Ft. Collins, CO 80523

E-mail - crmartin@lamar.colostate.edu

I. Introduction.

Nanomaterials constitute an emerging subdiscipline of the chemical and materials sciences that deals with the development of methods for synthesizing nanoscopic particles of a desired material and with scientific investigations of the nanomaterial obtained (1-6). Nanomaterials have numerous possible commercial and technological applications including uses in analytical chemistry (7-10), electronic, optical and mechanical devices (1,2,11), drug-delivery (12), and bioencapsulation (13). In addition, this field poses an important fundamental philosophical question - how do the properties (e.g., electronic, optical, magnetic) of a nanoscopic particle of a material differ from the analogous properties for a macroscopic sample of the same material?

There are now numerous chemical methods for preparing nanomaterials (2,3,11). Our research group has been exploring a method we call "template-synthesis" (3-6). This method entails synthesizing the desired material within the pores of a porous membrane or other solid. The membranes employed have cylindrical pores of uniform diameter (Figure 1). In essence, we view each of these pores as a beaker in which a particle of the desired material is synthesized. Because of the cylindrical shape of these pores, a nanocylinder of the desired material is obtained in each pore. Depending on the material and the chemistry of the pore wall, this nanocylinder may be solid (a fibril or nanowire, Figure 2A) or hollow (a tubule, Figure 2B).

The template method has a number of interesting and useful features. First, it is a very general approach; we have used this method to prepare tubules and fibrils composed of electronically conductive polymers, conventional insulating polymers, metals, semiconductors, carbons, and Li^+-intercalating materials (3-6). Furthermore, nanostructures with extraordinarily small diameters (<10 nm) can be prepared (14). Because the pores in the membranes used have monodisperse diameters, analogous monodisperse nanostructures are obtained. Finally, the tubular or fibrillar nanostructures synthesized within the pores can be freed from the template membrane and collected (Figure 2B). Alternatively, an ensemble of nanostructures that protrude from a surface like the bristles of a brush can be obtained (Figure 2A).

Nanomaterials and electrochemistry have a long shared history, for example, the use of finely dispersed Pt particles as catalysts in fuel cell electrodes. This chapter, however, deals specifically with applications of template-synthesized nanomaterials in electrochemistry. Three possible applications of are discussed. The first entails use of the template method for preparing ensembles of nanoscopic electrodes. The second application concerns the development of a new type of ion-permselective membrane - the metal nanotubule membrane. These membranes can be viewed as universal ion exchanges as they can be reversibly electrochemically switched between cation permselective, anion permselective and non-permselective states. The final application reviewed here entails the use of the template method to prepare monodisperse nanoparticles of Li^+-intercalation materials for possible use as electrodes in Li^+ batteries.

II. Ensembles of Nanoscopic Electrodes.

Electrochemistry at electrodes with nanoscopic dimensions constitutes one of the most important frontiers in modern electrochemical science (see ref. 15, and references therein). Such electrodes offer a myriad of opportunities including the possibility of doing electrochemistry in highly resistive media and the possibility of investigating the kinetics of redox processes that are too fast to study at electrodes of conventional dimensions. We have used the template method to prepare ensembles of nanoscopic Au disk electrodes where the electrode elements have diameters as small as 10 nm (15).

A. Experimental.

1. Template Membranes. Nanoelectrode ensembles (NEEs) were prepared by electroless deposition of Au within the pores of polycarbonate membrane filters (Poretics). Filters with pore diameters of 10 nm and 30 nm were used. The pore densities and average center-to-center distances between pores for these membranes are shown in Table I. Multiplying the pore density (pores cm^{-2}) by the cross-sectional area of a single pore (cm^2 per pore), provides a parameter called the fractional pore area (15) (Table I). This is an important parameter because, assuming that each pore produces an active nanodisk electrode, the fractional pore area is equivalent to the fractional electrode area, which is the sum of the areas of the Au-nanodisk elements in the NEE divided by the geometric area of the NEE. We have shown that the fractional electrode area can be determined experimentally from the double layer charging currents obtained at the NEE (15-18). Ideally, this experimental fractional electrode area and the fractional pore area should be equivalent (Table I).

2. Electroless Au Deposition. Electroless metal deposition involves the use of a chemical reducing agent to plate a metal from solution onto a surface. The key requirement is to arrange the chemistry such that the kinetics of homogeneous electron transfer from the reducing agent to the metal ion are slow. A catalyst that accelerates the rate of metal ion reduction is then applied to the surface to be coated. In this way, metal ion is reduced only at the surface, and the surface becomes coated with the desired metal. The thickness of the metal film deposited can be controlled by varying the plating time.

The electroless plating process has been described previously (15). Briefly, a "sensitizer" (Sn^{2+}) is first applied to the surfaces (pore walls plus faces) of the template membrane. This is accomplished by simply immersing the membrane into a solution containing $SnCl_2$. The Sn^{2+}-sensitized membrane is then activated by immersion into an aqueous $AgNO_3$ solution. This causes a redox reaction in which the surface-bound Sn(II) gets oxidized to Sn(IV) and the Ag^+ gets reduced to elemental Ag. As a result, the pore walls and membrane faces become coated with discrete, nanoscopic Ag particles. The Ag-coated membrane is then immersed into an Au plating bath. The Ag particles are galvanically displaced by Au, and the pore walls and faces become coated with Au particles. These particles catalyze the reduction of Au(I) on the membrane surfaces using formaldehyde as the reducing agent.

The plating process is continued until solid Au nanowires are obtained in each pore. In addition, both faces of the membrane become coated with Au films. For the NEE application, one of these surface Au films is removed using a simple Scotch-tape method (15). This exposes the ends of the Au nanowires that are embedded within the pores of the membrane. These Au disks constitute the electrode elements of the NEE. Electrical contact is made to the Au surface film that was left in tact on the opposite face of the membrane. By applying a potential to this Au surface film (relative to a reference electrode immersed into the same solution) redox reactions can driven (in parallel) at the ensemble of Au nanodisks. Details of the NEE fabrication procedure have been described previously (15).

It is important to point out that if plating is terminated before solid Au nanowires are obtained, an Au nanotubule that spans the complete thickness of the template membrane is deposited within each pore. We have shown that these nanotubule membranes have interesting ion-transport properties (19). This will be subject of the following section of this chapter.

B. Characterization of the NEEs.

1. Electron Microscopy and Optical Absorption Spectroscopy. The key feature of the electroless deposition process is that Au deposition begins at the pore wall. As a result, after brief deposition times, a hollow Au tubule is obtained within each pore (19). These tubules can be imaged by taking transmission electron micrographs of microtomed sections of the tubule-containing membrane. An image of this type for a membrane that contained 50 nm-diameter pores is shown in Figure 3. The Au tubules (black rings) appear elliptical (and ragged) due to distortion by the microtoming process. Scanning electron microscopy can also be used to image the face of the membrane in order to see the individual Au nanodisk electrode elements (15). However, the 10 nm Au disk size can push the limits of resolution of a conventional scanning electron microscope.

Nanometals have interesting optical properties (20-22). For example, suspensions of nanoscopic Au particles can be pink, purple or blue depending on the diameter of particles (22). These colors arise from the plasmon resonance absorption of the nanometal particle, a phenomenon we have explored in some detail (20,21). We have shown that membranes containing Au nanowires like those described here also show this plasmon resonance band, and as a result, such membranes can show a wide variety of colors. This absorption in the visible region provides an interesting optical approach for characterizing the Au nanowire-containing membranes.

Figure 4 compares absorption spectra for membranes containing 10 nm-diameter and 30 nm-diameter Au nanowires. The wavelength of maximum absorption intensity for the membrane containing the 10 nm-diameter nanowires is blueshifted relative to that for the membrane containing the 30 nm-diameter nanowires. This blueshift for the smaller diameter nanowires is in qualitative agreement with the predictions of effective medium theory (20,21).

As would be expected from the spectra shown in Figure 4, the membranes containing the 10 nm-diameter nanowires appear pink in color whereas the membranes containing the 30 nm-diameter nanowires are purple. Because of these distinctive colors, it is easy to distinguish the 30 nm disk-diameter NEEs (30NEEs) from the 10 nm disk-diameter NEEs (10NEEs).

2. Double-layer charging currents. A persistent problem with micro- and nanoelectrodes is the sealing of the conductive element to the insulating material that surrounds the element such that solution does not creep into this junction (15,16,23). This solution creeping is undesirable because it causes the double layer charging currents to be spuriously large. Previous methods for improving the seal have included silanization of the surrounding insulator (23) and impregnating the junction between the electrode and the insulating material with low molecular weight polyethylene (16). However, neither of these methods have proven completely satisfactory. We have recently introduced a superior method for sealing the junction between the Au nanowires and the polycarbonate host membrane (15). This method exploits the heat-shrinkability of the template membrane.

The polycarbonate membranes are stretch-oriented during fabrication in order to improve their mechanical properties. If the membrane is subsequently heated above its glass-transition temperature (~150° C), the polymer chains relax to their unstretched conformation, and the membrane shrinks. This shrinking of the membrane around the Au nanowires in the pores causes the junction between the nanowire and the pore wall to be sealed. This is illustrated in Figure 5, which shows voltammograms for trimethylaminomethylferrocene ($TMAFc^{+}$) before (Figure 5A) and after (Figure 5B) the heat-treatment procedure. Before heat treatment, the double layer charging currents are pronounced. After heat treatment, the charging currents are not discernible at the current-sensitivity setting used.

We have used voltammetric measurements in the absence of the electroactive species to quantitatively evaluate this heat-sealing procedure. The magnitude of the double layer-charging current can be obtained from these voltammograms (15-18), and this allows for a determination of the fractional electrode area (Table I). This experimental fractional electrode area can then be compared to the fractional pore area calculated from the known pore diameter and density of the membrane (Table I). In order to use this method, the double layer capacitance of the metal must be known. The double layer capacitance of Au was determined from measurements of charging currents at Au macro-disks electrodes of known area (Figure 6, curve a) . A value of 21 μF cm^{-2} was obtained.

Figure 6 compares double layer charging currents obtained at a 10NEE, a 30NEE, and an Au macro-disk electrode with active area equal to the geometric areas of the NEEs. As would be expected the charging currents at the NEEs are significantly lower than at the macro-disk electrode. The fractional electrode areas obtained from the double layer charging currents at the NEEs are shown in Table I. The fractional electrode area for the 30NEE is, within experimental error, identical to the fractional pore area (Table I). This indicates that each of the pores is filled with a Au nanowire and that the heat-shrinking procedure used to seal these 30 nm-diameter nanowires is quite effective.

The fractional electrode area at the 10NEE is within a factor of two of the fractional pore area. This larger-than-expected fractional electrode area may result from a small amount of solution leakage around the 10 nm-diameter Au nanowires. The alternative possibility is that the pore density and/or pore size determined by electron microscopy is incorrect. This is a likely possibility because, as indicated above, it is difficult to image 10 nm structures using a conventional scanning electron microscope. Given the general observation that the sealing problem for a micro- or nanoelectrode becomes worse as the diameter of the electrode decreases (16,23), the agreement between the fractional electrode areas and the fractional pore areas (Table I) is satisfactory.

C. Faradaic Electrochemistry at the NEEs. The nature of the Faradaic currents observed at a NEE depend on the distance between the electrode elements and the time scale (i.e., scan rate) of the experiment (15). These NEEs operate in the "total-overlap" response regime at the scan rates used here. In this total-overlap regime, the diffusion layers at the individual elements of the NEE have overlapped to produce a diffusion layer that is linear to the entire geometric area of the NEE (15). As a result, conventional peaked-shaped voltammograms are obtained. Indeed, for the reversible case, the voltammogram at a NEE operating in this total-overlap regime should be identical to the voltammogram obtained at a macro-disk electrode with active area equivalent to the geometric area of the NEE.

Experimental and simulated cyclic voltammograms for a solution that was 5 μM in $TMAFc^+$ and 0.5 mM in supporting electrolyte (sodium nitrate) are shown in Figure 7 (15). The experimental data were obtained at a 10NEE. In agreement with the above discussion, the experimental voltammograms are peak shaped and peak current increases with the square root of scan rate. This latter point is proven by the agreement between the experimental and simulated voltammograms. The simulated data were obtained by assuming reversible electrochemistry at a macro-disk electrode with active area equivalent to the geometric area of the NEE. Other than assuming an arbitrarily high value for the standard heterogeneous rate constant, there are no adjustable parameters in these simulations. The quantitative agreement between the experimental and simulated voltammograms indicates that the reversible, total-overlap limiting case is, indeed, operative at this NEE.

Three other comments are worth making regarding the data in Figure 7. First, the concentration of both the electroactive species (5 μM) and the supporting electrolyte (0.5 mM) are low. Low concentrations were used because we have discovered an interesting effect of supporting electrolyte concentration on the electrochemistry observed at the NEEs (see below). Second, it is possible that such low supporting electrolyte concentrations exacerbate problems of uncompensated solution resistance. At the concentration of electroactive species and the scan rates used here, the current at the NEEs are low (e.g. less than 100 nA in Figure 7). As a result, uncompensated solution resistance distorts the voltammograms to a negligible extent, even at the mM supporting electrolyte concentrations used here. Indeed, voltammograms with and without application of 90% iR compensation are identical (15).

Third, the experimental voltammograms in Figure 7 have not been corrected for background currents. Nevertheless, the agreement between the experimental and simulated voltammograms (where only Faradaic currents are simulated) is good. Background subtraction is not necessary, at these scan rates, because the double layer charging currents at the NEEs are orders of magnitude lower than at a macro-electrode of equivalent geometric area (Figure 6). Because the Faradaic currents at the NEE and the macro-electrode are, for the reversible case, identical (Figure 7), this diminution in the background currents also means the signal-to-background ratio at the NEE is orders of magnitude larger than at the macro-electrode. This point will be explored further below. It is this enhancement in signal-to-background ratio that allows us to use such low concentrations of electroactive species.

So far we have discussed only the reversible case. The equivalence of the net Faradaic current at the NEE and at a macro-electrode of the same geometric area (Figure 7) means that the flux at the individual elements of the NEE are many orders of magnitude larger than the flux at the macro-electrode. Indeed, the experimentally-determined fractional electrode areas (Table I) indicate that, for the reversible case, the flux at the elements of a 10NEE will be ~1000 times higher than at the macro-electrode; the flux at the elements of the 30NEE will be ~250 times higher. The higher fluxes at the NEE elements means that the NEEs will be more sensitive to the kinetics of electron transfer than a macro-electrode (15).

The simplest way to think about this situation is that for any redox couple, the quasireversible case can be observed at a NEE at much lower scan rates than at a macro-electrode. Indeed, because flux is related to the square root of scan rate, the 10^3-fold enhancement in flux at the 10NEE means that one would have to scan a macro-electrode at a scan rate 10^6 times higher in order to obtain the same kinetic information obtainable at the NEE. That is, if for a particular redox couple one observed quasireversible voltammetry at the 10NEE at scan rates above 1 V s^{-1}, one would have to scan at rates above 10^6 V s^{-1} to achieve the quasireversible case for this couple at a macro-electrode. This ability to obtain kinetic information at dramatically lower scan rates is an important advantage of a NEE.

The $Ru(NH_3)_6^{3+/2+}$ voltammograms (Figure 8) illustrate this point. The standard heterogeneous rate constant for this couple has been measured by a number of groups; values of 0.26 (24), 1.8 (25), and 76 (26) cm s^{-1} have been reported. Assuming, for the sake of illustration, a value of 1 cm s^{-1}, Nicholson's theory shows that quasireversible $Ru(NH_3)_6^{3+/2+}$ voltammograms will be obtained, at a macro-electrode, at scan rates above ~5 V s^{-1} (27) .

Figure 8A shows voltammograms at various scan rates for $Ru(NH_3)_6^{3+/2+}$ at a 30NEE. This couple shows reversible voltammetry (ΔE_{pk} ~59 mV) at the lowest scan rates shown, but the voltammograms become quasireversible at scan rates above 0.01 V s^{-1}. Therefore, as expected, the transition to quasireversible behavior is observed at dramatically lower scan rates at the 30NEE than would be observed at a macro-electrode. It is again important to emphasize that the increase in ΔE_{pk} observed is not due to uncompensated solution resistance (15).

Because the fractional electrode area at the 10NEE is lower than at the 30NEE (Table I), the transition to quasireversible behavior would be expected to occur at even lower scan rates at the 10NEE. Voltammograms for $Ru(NH_3)_6^{3+/2+}$ at a 10NEE are shown in Figure 8B. At the 10NEE it is impossible to obtain the reversible case, even at a scan rate as low as 5 mV s^{-1}. The effect of quasireversible electrochemistry is clearly seen in the larger ΔE_{pk} values and in the diminution of the voltammetric peak currents at the 10NEE (relative to the 30NEE, Figure 8). This diminution in peak current is characteristic of the quasireversible case at an ensemble of nanoelectrodes (25,28). These preliminary studies indicate that the response characteristics of the NEEs are in qualitative agreement with theoretical predictions (25,28).

D. Electroanalytical detection limits at the NEEs. For the reversible case, the voltammetric detection limit for a redox species at a NEE should be the detection limit for the same species at the corresponding macro-electrode multiplied by the fractional electrode area (Table I) of the NEE (15). Because the fractional electrode area for the 10NEE is ca. 10^{-3}, this suggests that the voltammetric detection limit at a 10NEE should be three orders of magnitude lower than the detection limit obtained at a macro-electrode. Figure 9A shows voltammograms at a macro-electrode at various low concentrations of $TMAFc^+$.

As would be expected, the Faradaic signal ultimately vanishes into the background double-layer-charging currents. Taking a total measured current that is twice the background charging current as the criterion for establishing the detection limit (15), these voltammograms show that the detection limit for $TMAFc^+$ at the macro-electrode is 1.6 μM.

Voltammograms for various low concentrations of $TMAFc^+$ at a 10NEE are shown in Figure 9B. While the voltammograms look nearly identical to those obtained at the macro-electrode, the concentrations are three orders of magnitude lower. Using the same criterion for the detection limit, we obtain a detection limit at the 10NEE that is three orders of magnitude lower (1.6 nM) than at the macro-electrode. It is gratifying that the experimentally-observed enhancement in detection limit at the NEE is exactly as would be predicted from the fractional electrode area data in Table I.

Cyclic voltammetry is generally considered to be a poor electroanalytical technique. This is because the high double-layer charging currents observed at a macro-electrode make the signal-to-background ratio low. The voltammograms in Figure 9B clearly show that at the NEEs, cyclic voltammetry is a very powerful electroanalytical technique. There is, however, a caveat. Because the NEEs are more sensitive to electron transfer kinetics, the enhancement in detection limit that is in principle, possible, could be lost for couples with low values of the heterogeneous rate constant. This is because one effect of slow electron transfer kinetics at the NEE is to lower the measured Faradaic currents (e.g., Figure 8).

This sensitivity to slow electron transfer kinetics could, however, prove to be an advantage in sensor applications where a mediator, with fast electron transfer kinetics, is used to shuttle electrons to a redox enzyme (29). Chemical species that are electroactive in the same potential region as the mediator can act as interferants at such sensors. If such an interfering electroactive species shows slow electron transfer kinetics, it might be possible to eliminate this interference at the NEE. This is because at the NEE, the redox wave for the kinetically-slow interferant might be unobservable in the region where the kinetically-fast mediator is electroactive. We are currently exploring this possibility.

E. The Effect of Supporting Electrolyte. As indicated above, all of the experimental data reported thus far were obtained at low concentrations of both supporting electrolyte (mM) and electroactive species (µM). This was done because we have observed an interesting effect of supporting electrolyte concentration on the shape of the voltammetric waves observed at the NEEs (15). We have found that the reversibility of the voltammetric waves for all couples investigated to date ($TMAFc^{+/2+}$, $Ru(NH_3)_6^{3+/2+}$, $Mo(CN)_8^{4-/3-}$) improves as the concentration of supporting electrolyte decreases. This effect is illustrated, for $TMAFc^{+/2+}$ in Figure 10. Note that the peak currents decrease and the ΔE_{pk} values increase as the concentration of supporting electrolyte increases.

This effect has been observed in all of the supporting electrolytes we have investigated to date; these include $NaNO_3$, $NaClO_4$, Na_2SO_4, Et_4NBF_4, Et_4NClO_4, $Mg(NO_3)_2$, KNO_3, KPF_6, $ZnSO_4$, and pH = 7.0 phosphate buffer. Furthermore, this effect is reproducible and reversible. By reversible we mean that if the NEE is taken out of a solution with high supporting electrolyte concentration (e.g., 50 mM) and returned to a solution with low electrolyte concentration (e.g., 1 mM), the voltammetric wave immediately assumes the reversible appearance characteristic of the low electrolyte-concentration solution (Figure 10). Furthermore, we have observed this effect for NEEs prepared from both polycarbonate and polyester membranes, for NEEs prepared from membranes with and without the PVP that is used to improve membrane wettability, and for NEEs with low densities of electrode elements (18) where total overlap does not occur (30).

F. Conclusions. We have demonstrated a new method for preparing electrodes with nanoscopic dimensions. We have used this method to prepare nanoelectrode ensembles with individual electrode-element diameters as small as 10 nm. This method is simple, inexpensive, and highly reproducible. The reproducibility of this approach for preparing nanoelectrodes is illustrated by the fact that NEEs given to other groups yielded the same general electrochemical results as obtained in our laboratory (31). These NEEs display cyclic voltammetric detection limits that are as much as three orders of magnitude lower than achievable at a conventional macro-electrode.

III. Gold Nanotubule Membranes with Electrochemically-Switchable Ion-Transport Selectivity.

The electroless plating method described above was used to prepare membranes that contain cylindrical gold nanotubules that span the complete thickness of the membrane. The inside radius of the nanotubules can be varied at will; nanotubule radii as small as 0.8 nm are described here. These metal nanotubule membranes show selective ion-transport analogous to that observed in ion-exchange polymers (32). Ion permselectivity (33) occurs because excess charge density can be present on the inner walls of the tubules. The tubes reject ions of the same sign, and transport ions of the opposite sign, as this excess charge. This is only possible when the inside radius of the tubule is small relative to the thickness of the electrical double layer (34) within the tubule. These membrane can be either cation selective or anion selective, depending on the potential applied to the membrane. Hence, these metal nanotubule membranes can be viewed as universal ion exchange membranes.

A. Preparation of the Au Nanotube Membranes (19). The pores in a commercially available polycarbonate filtration membrane (Poretics) were used as templates to form the nanotubules (pore dia = 50 nm, pore density = 6×10^8 pores cm^{-2}, thickness = 6 μm). As before, the electrolessly plated Au deposits both on the pore walls and the membrane faces. The gold surface layers on the membrane faces allow us to make electrical contact to the Au nanotubules within the pores. The thickness of the gold layers deposited on the pore walls can be controlled by varying the plating time. As a result, the inside radius of the gold nanotubules can be varied at will (as determined from measurements of gas (He) flux (35) across the tubule-containing membrane).

B. Results. We describe the results of three sets of experiments that demonstrate that these Au nanotubule membranes can show selective ion transport. All of these experiments involve a U-tube cell in which the membrane to be studied separates two aqueous solutions. The simplest experiment entails using a "feed" solution of a colored anionic or cationic species on one side of the membrane and a "receiver" solution that is initially devoid of the colored species on the other side of the membrane. A membrane that contained ~ 2.5 nm radii (35) Au nanotubules was used for these experiments.

When the feed solution is 1 mM in KCl and 0.5 mM in the cationic dye methylene blue, and the receiver solution is 1 mM KCl, the initially-colorless receiver solution turns blue due to transport of the cationic dye across the membrane (19). In contrast, when the feed solution is 1 mM in KCl and 5 mM in $KMnO_4$ (MnO_4^- is red), and the receiver solution is 1 mM KCl, the receiver solution remains colorless (19). These experiments provide simple visual evidence that this membrane transports a large cation but does not transport a much smaller anion. We have used potentiometric measurements to explore the nature of this cation permselectivity.

The extent of ion permselectivity displayed by a membrane can be expressed quantitatively by the transference numbers (36) for cations (t_+) and anions (t_-) within the membrane. Transference numbers can be determined potentiometrically by using a concentration cell (36), in which the membrane to be evaluated separates two electrolyte solutions that contain the same salt but at different concentrations. For a 1:1 salt, the membrane potential (E_m) is given by

$$E_m = (2.303RT/nF)(t_+ - t_-) \log(a_h/a_l) \qquad (1)$$

where a_h and a_l are the activities of the salt in the solution of high and low salt concentration, respectively (33). Equation 1 indicates that for an ideal cation-permselective membrane ($t_+ = 1.0$), a plot of E_m versus $\log(a_h/a_l)$ would be linear with an intercept of 0 and a slope of 59 mV (dashed line, Figure 11).

A concentration cell was assembled in which a gold-nanotubule membrane separated two KCl solutions. The potential of the membrane was not controlled with a potentiostat. However, Cl^- adsorbs strongly to gold (37), and the gold films on the membrane faces and the inside walls of the gold tubules have excess negative (Cl^-) charge on their surfaces. This excess negative charge is balanced by a layer of excess positive charge (K^+) in the solution immediately adjacent to gold surfaces (the electrical double layer) (34).

Data obtained from this concentration cell (Figure 11) show that these membranes can show ideal cation-permselective behavior and that the region over which ideal behavior is observed is extended to higher salt concentrations as plating time increases. These observations can be explained as follows: Over the range of plating times used in Figure 11, the average inside radii of the gold tubules varied from ~ 9.4 nm (60 min plating time) to ~0.8 nm (180 min plating time). Gouy-Chapman theory (34) predicts that over the salt concentration range used here, the thickness of the electrical double layer within the tubules (as approximated by the Debye length) varies from ~30 nm (lowest concentration) to ~0.3 nm (highest concentration). Figure 11 indicates that the gold nanotubule membranes show ideal cation permselectivity, provided the radius of the tubule is small relative to the thickness of the electrical double layer within the tubule.

To illustrate this point, consider the membrane plated for 60 min. The tubules in this membrane are on average ~9.4 nm in inside radius. At low concentrations of salt, the electrical double should be thicker than this tubule radius. Anions are excluded from the tubes, and ideal cation permselectivity is observed. At high salt concentrations, the electrical double layer is thin relative to the tubule radius. Anions can now enter the tubules and ideal cation permselectivity is lost (Figure 11). Finally, the membrane plated for 180 min shows cation permselectivity almost identical to that of the ionomer Nafion® (38), which is a highly cation-permselective polymer used in industrial electrolytic processes (32).

We consider now the idea of controlling the permselectivity by potentiostatically injecting excess charge into the gold nanotubules. For these studies, it is essential to use an anion that does not adsorb to gold because we do not want the excess charge to be determined by adsorption. Because F^- does not adsorb to Au (39), KF was chosen as the electrolyte. A concentration cell was assembled in which a gold nanotubule membrane separated solutions that were 1 mM and 10 mM in KF. This membrane was connected (through the Au surface layers) to the working electrode lead of a potentiostat and the potential applied to the membrane was varied over the range from -0.5 V to +0.5

V verses Ag/AgCl. The E_m values were measured at each applied potential (Figure 12).

The dashed lines at the top and bottom of Figure 12 are the E_m values that would be achieved if the nanotubule membrane showed ideal cation and ideal anion permselectivity, respectively (Eq. 1). At negative applied potentials, the nanotubule membrane shows ideal cation permselectivity, whereas at positive applied potentials the membrane shows ideal cation permselectivity. This selectivity occurs because at negative applied potentials, excess electrons are present on the walls of the tubes, and excess positive charge (K^+) accumulates within the tubes. As a result, anions (F^-) are excluded and cations (K^+) are transported by the membrane. At positive applied potentials the opposite situation occurs, and cations are excluded and anions are transported.

For any combination of metal and electrolyte, there is a potential called the potential of zero charge (pzc) where there is no excess charge on the metal. At this potential the nanotubule membranes should show neither cation nor anion permselectivity, and E_m should approach (40) 0 mV. E_m for the tubule-containing membrane does, indeed, go from the ideal cation permselective value, through zero to the ideal anion permselective value (Figure 12). Furthermore, the potential at which E_m approaches (40) zero is close to the reported pzc [-4 mV for Au in 1 mM NaF (41)].

Figure 12 shows that the gold nanotubule membranes can function as electronically switchable ion exchange membranes. However, it would seem that this would only be possible if the electrolyte contained only nonadsorbing anions such as F^-. If an adsorbing anion (such as Cl^- or Br^-) (37,42) were present, it would adsorb at positive applied potentials yielding a cation permselective membrane. While the anion would not adsorb at sufficiently negative applied potentials, the metal would have excess electron density at such potentials, and, again, cation permselectivity would be observed. Hence, in the presence of an adsorbing anion, cation permselectivity will be observed at all applied potentials (19).

Anion adsorption can be prevented by adsorbing a monolayer of a strongly adherent thiol molecule to the Au surfaces (43,44). 1-Propanethiol (PT) was used here because the gold nanotubules can still be wetted with water after adsorption of the PT monolayer (44). The E_m verses applied potential curves for an untreated and PT-treated gold nanotubule membrane, with KBr solutions present on either side of the membrane, are shown in Figure 13. The untreated membrane shows only cation permselectivity, but the permselectivity of the PT-treated membrane can be switched, exactly as was the case with the nonadsorbing electrolyte (Figure 12).

C. Conclusions. We have demonstrated that these metal nanotubule membranes can be cation permselective, anion permselective or nonselective, depending on the potential applied to the membrane (45). These membranes can be as permselective as the commercially-important Nafion® polymer and should have applications in both fundamental and applied electrochemistry. In addition, because the gold tubules have radii that approach molecular dimensions, these membranes might have applications in chemical separations. For example, we have recently shown that these membranes can be used to separate molecules on the basis of size (46).

IV. Nanomaterials in Secondary Battery Research and Development.

The need to develop high rate-performance electrodes (47) in advanced batteries, such as rocking-chair or lithium-ion type cells (48), has led to efforts to reduce the effects of mass-transfer during discharge/charge (49-51). Mass-transfer effects are caused by the slow diffusion, and long diffusion distances, of

Li^+ in the Li^+-intercalation materials used as the battery electrodes (49-51). For example, Auborn and Barberio (51) showed that lithium-ion battery performance is dramatically affected by the particle size of the Li^+-intercalation materials used to prepare the electrodes. Specifically, when large particles were used, the experimental capacity of the electrode was significantly lower than the theoretical capacity. Tipton et al also discuss this effect of particle size on discharge capacity (49).

Capacity is lost when large particles are used to make the electrode because concentration polarization occurs within the particle before the entire capacity can be utilized (49-53). Auborn and Barberio obviated this problem by decreasing the particle size. This not only lowered the current density, but lowered the diffusion distances of Li^+ within the electrode material (49,50), thus delaying the onset of concentration polarization. As a result, a larger fraction of the theoretical capacity of the electrode could be utilized (50-53). Whittingham (54) also showed that utilization of the cathode capacity for a Li/TiS_2 battery was influenced by the size of TiS_2 particles. Theoretical analyses also point out the importance of particle size (52,53).

Given the importance of particle size to rate capabilities in Li^+ batteries, preparation of nanostructures of Li^+-insertion-material for possible use as electrodes in Li^+ batteries seemed like an obvious extension of our work on nanomaterials. The fact that these nanostructures can be prepared as high-density ensembles that protrude from a surface like the bristles of a brush (Figure 2A) seemed particularly useful for this proposed application because the substrate surface could then act as a current collector for the nanostructured battery electrode material.

We have proven that electrodes based on such ensembles of template-synthesized Li^+-insertion micro- and nanomaterials have superior rate capabilities relative to thin film electrodes composed of the same material. Specifically, these nanostructured electrodes can deliver higher capacities at high discharge currents than can the same amount of a thin film of the same material. We have proven this superior performance for nanostructures composed of two different Li^+ insertion materials - $LiMn_2O_4$ and TiS_2. This work demonstrates that the fundamental issues that make nanomaterials scientifically interesting can be applied to the area of electrochemical energy production leading to a new hybrid field of research/technology. Results of our investigations of template-synthesized Li^+ battery electrode materials are reviewed here.

A. Investigations of Nanotubules of $LiMn_2O_4$.

1. Electrode Fabrication. This work was done in collaboration with Prof. Hiroshi Yoneyama of Osaka University (55). The procedure used to prepare the $LiMn_2O_4$ tubules is shown schematically in Figure 14. A commercially-available alumina filtration membrane (Anopore, Whatman) was used as the template. This membrane contains ~200 nm-diameter pores, is 60 μm thick, and has a porosity of ~0.6. A 1.5 cm x 1.5 cm piece of this membrane was mounted on a Pt plate (2 cm x 2 cm) by applying a strip of plastic adhesive tape (also 2 cm x 2 cm, NICHIBAN VT-19) across the upper face of the membrane. The Pt plate will serve as the current collector for the $LiMn_2O_4$ battery-electrode material. The strip of tape, which will be subsequently removed, had a 1.0 cm^2 circular hole punched in it which defined the area of the membrane used for the template synthesis of the LiMn2O4.

The Pt current collector was first used to deposit short (~2 μm) Pt nanoposts (20,21) into the template membrane (Figure 14A) (55). These Pt nanoposts anchor the alumina membrane to the Pt surface and will serve to make electrical contact to the $LiMn_2O_4$ nanotubes. After Pt deposition, the pores in the membrane were filled with an aqueous solution that was 0.5 M in $LiNO_3$, and 1 M in $Mn(NO_3)_2$ (Figure 14B). The excess solution was wiped from the membrane surface, and the solvent (water) was removed by heating (50° C) in vacuum for 1 hr. The assembly was then heated at 500° C in air for 5 hours. This burns away the plastic tape and also causes tubules of $LiMn_2O_4$ to form within the pores (Figure 14C, Figure 15).

The alumina template was then dissolved away using 2 M NaOH, and the resulting array of nanotubes (Figure 1D) was heated at 850° C in air for 24 hours. X-ray diffraction studies indicate that this yields the spinel $LiMn_2O_4$ (55). The amount of $LiMn_2O_4$ deposited was determined by dissolving the nanotubes and using a visible absorption assay for MnO_4^- in the resulting solution (55). This assay showed that 0.75±0.03 mg of $LiMn_2O_4$ tubules were deposited into the 1 cm^2 portion of the template membrane.

The final step entailed coating both the inner and outer surfaces of the $LiMn_2O_4$ tubules with the conductive polymer polypyrrole (56). It has been shown that such $LiMn_2O_4$/polypyrrole composite electrodes have lower resistance and higher capacity than electrodes prepared from $LiMn_2O_4$ alone (56). Furthermore, the high porosity and fast (relative to $LiMn_2O_4$) electrochemical kinetics insure that all of the surfaces of the nanotubules remain accessible to solvent and electrolyte. The polypyrrole coat was deposited by simply applying 5 µL of a solution that was 1 M in $HClO_4$ and 0.2 M in pyrrole to the $LiMn_2O_4$ surface. This results in oxidative polymerization of all of the pyrrole, yielding 0.065 mg of polypyrrole per cm^2 of Pt substrate surface (56).

In order to determine whether the new nanotubule electrode shows improved performance, a control electrode composed of the same material, but prepared via a more conventional method, is required. This control $LiMn_2O_4$

electrode was prepared by applying the precursor solutions described above directly onto a 1 cm^2 Pt plate and thermally processing as before. Scanning electron micrographs showed that these films consisted of $LiMn_2O_4$ particles with diameters of ~500 nm (55). Spectrophotometric assay showed that this control electrode also contained 0.75 mg of $LiMn_2O_4$ per cm^2. A polypyrrole coat, identical to that applied to the tubular electrode (0.065 mg), was also applied to this control electrode.

2. Electron Microscopy. Figure 15 shows a scanning electron micrograph of a typical ensemble of $LiMn_2O_4$ nanotubules. The outer diameter of these tubes is determined by the diameter of the pores (200 nm) in the template membrane; the tubule wall thickness is ~50 nm. Tubules are obtained because the salts preferentially adsorb to the alumina pore wall after removal of the water from the precursor salt solutions. This tubular structure insures that the electrolyte solution can access a large surface area of the $LiMn_2O_4$ electrode material. Furthermore, it is clear from the charge/discharge reactions for $LiMn_2O_4$ (Equation 2, below) that Li^+ must diffuse into and out of this material. The extremely thin walls of these nanotubules insure that the distance that Li^+ must diffuse within the $LiMn_2O_4$ phase is very small (~25 nm).

3. Charge/Discharge Experiments. Constant current charge/discharge experiments were carried out on both the nanotubular and control $LiMn_2O_4$ electrodes. The cell consisted of the $LiMn_2O_4$ working electrode, a Pt sheet counter electrode, and an Ag/AgCl reference electrode (propylene carbonate saturated with LiCl; 2.9 V vs. Li/Li^+; potentials quoted here are vs. Li/Li^+). The electrolyte was 1 M $LiClO_4$ dissolved in a 1:1 (by volume) mixture of propylene carbonate and 1,2-dimethoxyethane. The electrodes were charged to an upper potential limit of 3.8 V and discharged to a lower limit of 2.2 V. The charge/discharge reactions for this material can be written as (57)

$$LiMn_2O_4 + xLi^+ + x\,e^- \underset{\text{Charge}}{\overset{\text{Discharge}}{\rightleftarrows}} Li_xMn_2O_4 \qquad (2)$$

The value of x for the potential region used here is ca. 1; i.e.; the fully charged material is $LiMn_2O_4$ and the fully discharged material has the approximate stoichiometry $Li_2Mn_2O_4$. All measurements were done in an Ar-filled glove box.

Figure 16 shows charge/discharge curves (at a current density of 0.1 mA cm^{-2} of Pt current collector surface area) for nanotubular and control $LiMn_2O_4$ electrodes. The key question to be addressed from this figure is - what charge and discharge capacity can be achieved (for each type of electrode) before the potential limits for charging (3.8 V) and discharging (2.2 V) are obtained? Figure 16 clearly shows that both the charge and discharge capacity are higher for the nanotubular electrode than for the control electrode. This higher capacity is obtained in spite of the fact that both electrodes contain the same quantities of both $LiMn_2O_4$ and polypyrrole.

It is easy to show (55) that the polypyrrole present in these electrodes contributes 8.85×10^{-3} mAh to the total experimental discharge capacity. Furthermore, it is known that over the potential window used here, $LiMn_2O_4$ has a theoretical (maximum) capacity of 148.3 mAh g^{-1} (55) Correcting the experimental capacities in Figure 16 for the polypyrrole contribution and dividing by the mass of the $LiMn_2O_4$ used shows that in the nanotubular electrode 90 % (133.8 mAh g^{-1}) of the theoretical capacity is utilized, whereas in the control electrode only 37% (54.9 mAh g^{-1}) of the capacity is used. These data clearly show that the nanotubular electrode is superior to the control $LiMn_2O_4$ electrode.

It was noted, above, that a unique feature of the nanotubular electrode is the thin tubule walls which insure that the distance over which the Li^+ must diffuse within the $LiMn_2O_4$ is small. If this factor is partially responsible for the improved performance of the nanotubular electrode (vs. the control electrode), then the performance should be further improved at higher current densities. This is because higher current densities force the charge and discharge process to occur at higher rates, and this will exacerbate the problem of slow Li^+ diffusion within the $LiMn_2O_4$. Figure 17 shows that the performance of the tubular electrode (relative to the control) is, indeed, improved at higher current densities. At a current density of 1 mA cm^{-2}, the experimental capacity of the tubular electrode is over an order of magnitude higher than that of the control electrode.

Finally, the other factor which could contribute to the improved performance of the nanotubule electrode is its higher surface area. This higher surface area would make the true current density at the nanotubular material lower than at the control material. In order to access the contribution of surface area, BET measurements were made on both the nanotubular and control electrodes (55). The specific surface areas were found to be 40 m^2 g^{-1} (nanotubule electrode) and 13 m^2 g^{-1} (control electrode). This factor of three increase in surface area cannot account for the factor of 12 improvement in capacity observed at the highest current density (Figure 17). Hence, it is clear that the decreased diffusional distance in the nanotubular material plays a strong role in the improved performance of the nanotubular electrode.

B. TiS_2 Tubules Where Each Tube has its Own Built in Current Collector. The $LiMn_2O_4$ example discussed above provides proof of concept that a nanostructured Li^+-battery electrode can provide superior rate capabilities relative to a thin film electrode. We will show in this section that this concept applies to TiS_2 also. In addition, we will demonstrate a second interesting feature of the template-synthesis method. Specifically, we will show that by doing sequential template syntheses, it is possible to prepare composite structures in which outer tubules of the Li^+ intercalation material are coated onto concentric inner tubules of a metal. We have recently described a number of chemical strategies which can be used to prepare concentric tubular composite micro- and nanostructures (58). By coating tubes of TiS_2 over tubes of Au, each particle of the Li^+ intercalation material (the outer TiS_2 tube) has its own on-board current collector (the inner Au tube). This is important because, as illustrated by the $LiMn_2O_4$ example discussed above, the electronic conductivities of the Li^+-intercalation materials can often be too low. This work was done in collaboration with Professor Ellen R. Fisher of Colorado State University (59).

1. Electrode Fabrication. A schematic diagram of the fabrication method used is shown in Figure 18. The electroless plating procedure discussed above was used to deposit gold microtubules within the pores of the polyester template membrane. One gold surface layer was removed (Figure 18C) and the membrane was placed (remaining Au surface layer down) on a piece of Al foil (Figure 18D). The membrane was then dissolved by immersion of this assembly into hexafluoroisopropanol for 24 hours. This yielded an ensemble of Au tubules (0.9 μm o.d., 0.4 μm i.d.), protruding from the Au/Al substrate surface (Figure 18E and 19A). Interestingly, the adhesion between the Au film that was grown on the membrane and the substrate Al foil is very strong. This is evidenced by the fact that the membrane can be dissolved away without loss of the Au tubes from the Al/Au substrate. Furthermore, this assembly can be immersed into an electrolyte solution and electrochemical experiments run (see below) without loss of the Au tubes.

A home-built CVD reactor was then used to coat the outer TiS_2 tubules onto the inner Au tubules; details of the equipment and the synthesis have been described previously (59,60). TiS_2 was found to deposit as thin tubular skins on the outer surfaces of the Au microtubules; the thickness of the TiS_2 skin could be controlled by varying the deposition time (Figures 19B and C). The quantity of TiS_2 deposited was determined by dissolving the TiS_2 from the substrate and using inductively coupled plasma atomic emission analysis to determine the amount of Ti^{4+} in the resulting solution (59). Thin-film TiS_2 electrodes (control electrodes) were prepared by CVD of TiS_2 onto Al foil.

2. Electron Microscopy. Figure 19A shows an SEM image of the Au microtubules used as the current collector for the microstructured TiS_2 electrode. Note that a high density ensemble of monodisperse tubules is obtained. Figure 18B shows an analogous SEM image after CVD of TiS_2 onto the Au tubules (deposition time = 3 min) . The Au tubules have been coated with outer tubules of TiS_2. That the outer material is, indeed, TiS_2 was confirmed via energy-dispersive X-ray analysis and by X-ray diffraction (59,60). For this deposition time, the thickness of the walls of the outer TiS_2 tubes is ~360 nm. Figure 19C shows an SEM image after a longer TiS_2 deposition time (5 min). Note that the outer TiS_2 tubes now have thicker walls (~910 nm).

Figure 19D shows an SEM image of a CVD TiS_2 film that had been deposited on Au foil (deposition time = 2 min). The morphology of this TiS_2 is similar to that of the TiS_2 deposited on the Au microtubules. It is of interest to note, however, that when placed into electrolyte solution, such TiS_2 films deposited on Au foil detached from the Au-foil surface. In contrast, no detachment of TiS_2 was observed from the Au microtubular substrate. The enhanced roughness of the microtubular Au surface (Figure 19A) is undoubtedly responsible for this improved adhesion. Because TiS_2 detached form Au foil surfaces, electrochemistry on CVD TiS_2 films (the control electrodes) was done by depositing TiS_2 onto Al foil surfaces, where good adhesion was observed.

3. Electrochemical Experiments. A three-electrode cell - microtubular or control TiS_2 working electrode and Li foils as both the counter and reference electrodes - was used. The electrolyte was 1 M $LiClO_4$ in a 30:70 (v/v %) mixture of ethylene carbonate and diethyl carbonate. All electrochemical measurements were made in a glove box filled with argon. Au/TiS_2 composite microstructures with two different wall thicknesses for the outer TiS_2 tubes were investigated. These two different composite microstructures correspond to the images shown in Figure 19B and C. The thin-walled (~360 nm) TiS_2 tubules were obtained by using a 3 min deposition time (Figure 19B). These tubules contained 0.86 mg of TiS_2 per cm^2 of geometric surface area. (Geometric surface area is the area of the planer Al-foil substrate that supports the Au microtubules.) The thick-walled (~910 nm) TiS_2 tubules were obtained by using a 5 min deposition time (Figure 19C). These tubules contained 2.04 mg of TiS_2 per cm^2 of geometric surface area.

Cyclic voltammograms associated with the reversible intercalation of Li^+ (Equation 3) into the thick-walled TiS_2 tubules are shown in Figure 20.

$$TiS_2 + xe^- + xLi^+ \text{----------}> Li_xTiS_2 \qquad (3)$$

Voltammograms for a control electrode containing an essentially identical quantity of TiS_2 on a planar Al current collector are also shown. Note first the dramatically larger separation in peak potential (ΔE_{pk}) for the control electrode; this enhanced ΔE_{pk} is especially noticeable at the highest scan rate shown in Figure 20. Such large ΔE_{pk} values suggest that there is an uncompensated resistance element in the electrochemical circuit. To explore this point, voltammograms for the film electrode were obtained at various values of applied positive feedback. ΔE_{pk} decreased with increasing level of positive feedback (59). These data confirmed that uncompensated resistance does, indeed, contribute to the large ΔE_{pk} values seen in Figure 20.

The usual source of uncompensated resistance in a cyclic voltammetric experiment is solution resistance. Solution resistance is not, however, the source in this case (59). Li^+ intercalation entails diffusion of Li^+ into the TiS_2 lattice. The solid-state diffusion coefficient associated with this process is low (10^{-10} to 10^{-12} cm^2 sec^{-1}) (61). This low diffusion coefficient causes the ionic resistance of the film to be high, and it is this resistance that is responsible for the large ΔE_{pk} values (60). Hence, the low ionic diffusion coefficient for Li^+ within TiS_2 translates, electronically, into an unwanted ionic voltage drop across the TiS_2 film. This voltage drop is unwanted because, from a battery viewpoint, it lowers the output voltage of cell. Put another way, this film IR drop will causes a fraction of the energy produced by the battery to be dissipated (wasted) as resistive heat.

The ΔE_{pk} values for the microtubular electrode were found to be substantially smaller than for the equivalent (same quantity of TiS_2) control electrode (Figures 20). This indicates that the ionic resistance of the tubular TiS_2 film is less than that of the planer TiS_2 film. A lower resistance is obtained because the tubular films are thinner than the planer films. This is because the surface area of the microtubular current collector is 8 times higher than the surface area of the planar current collector. (This factor of 8x is calculated from the membrane thickness and the density and diameter of the pores in the membrane.) Since the control and microtubular electrodes contain the same amount of TiS_2, the factor of 8x higher underlying surface area of the microtubular electrode means that the TiS_2 film is effectively a factor of 8x thinner. These data point out the first advantage of the microtubular current collector concept - for equivalent amounts of TiS_2, the microtubular electrode will cause less of the energy output of the cell to be wasted as resistive heat.

Figure 21 shows analogous Li^+-intercalation voltammograms for the thin-walled TiS_2 tubular electrode and for a control electrode containing approximately the same amount of TiS_2. As would be expected, the magnitude of ΔE_{pk} for these thinner films is less than that for the thicker films.

It is interesting to also consider the role of slow electron transfer for these various TiS_2 electrodes . If the rate of electron transfer was infinitely fast, then applying positive feedback would cause ΔE_{pk} to decrease to the theoretical value for a reversible voltammogram (60 mV for a conventional diffusional voltammogram and 0 mV for a thin layer voltammogram). In fact, it proved impossible to decrease the experimental ΔE_{pk} values to these theoretical values by applying positive feedback (Figure 22). These data suggest that kinetic limitations are also contributing to the large ΔE_{pk} values obtained at these electrodes. Hence, we are in the regime of mixed kinetic and mass-transfer (in the TiS_2) control.

This is illustrated by the voltammograms shown in Figure 22. A tubular TiS_2 electrode, obtained after depositing TiS_2 for 3 min, was first cycled at a scan rate of 1 mV s^{-1}, with increasing amounts of applied positive feedback (Figure 22A). The ΔE_{pk} decreased from 375 mV (no positive feedback) to 100 mV (maximal positive feedback). This remaining (uncompensatable) peak splitting is due to slow kinetics. This is proven by the much lower scan rate voltammogram shown in Figure 22B. At this scan rate application of any positive feedback causes ringing indicating that film IR drop is now negligible. Furthermore, this low-scan rate voltammogram shows the symmetrical shape characteristic of finite diffusion within the tubular TiS_2 films (62). Note, however, that ΔE_{pk} (~35 mV) is greater than the theoretically-predicted 0 mV; this non-zero ΔE_{pk} value is caused by slow electron transfer kinetics (62).

Such kinetic limitations are also undesirable from the battery viewpoint because such limitations will cause the electrode to discharge at potentials lower than the theoretical values. This leads to the second important advantage of the microtubular current-collector concept. Because of the higher surface area, the current density at the tubular current collector will always be less than the current density at a planar current collector.

We turn now to the issue of concentration polarization to see if the microtubular current collector offers an advantage here also. The effect of concentration polarization was explored using both cyclic voltammetric and constant current discharge experiments. The voltammetric experiments entailed obtaining Li^+-intercalation voltammograms at increasing scan rates. The area under the forward wave corresponds to the discharge capacity of the electrode. In principle, a low scan rate region can be identified in which the discharge capacity is independent of scan rate. This means that over this timescale window, 100% of the experimental capacity of the electrode can be utilized. This is analogous to a constant-current discharge experiment at very low current density such that 100% of the capacity is utilized during the discharge. At high scan rates, the discharge capacity will ultimately decrease with increasing scan rate. This is analogous to a constant current discharge experiment at high current density where concentration polarization has occurred, and less than 100% of the capacity can be utilized.

Figure 23 shows the discharge capacities as function of scan rate for both the tubular and thin film TiS_2 electrodes that contain the larger amount of TiS_2. The theoretical capacity for TiS_2 (assuming a maximum intercalation level of one mole of Li^+ per mole of TiS_2) is 239 mA h g^{-1} (59). At the lowest scan rate employed, the experimental capacity for the control electrode is below this theoretical capacity, and capacity falls off sharply with increasing scan rate. These data show that the control electrode is suffering concentration polarization even at the lowest scan rates used here.

At the lowest scan rate employed, the microtubular electrode delivers an experimental capacity (256±21 mA h g^{-1}) that is identical to the theoretical capacity. These data show that concentration polarization is not a problem at the microtubular electrode at the lowest scan rate employed here. As scan rate is increased capacity does fall off, indicating the onset of concentration polarization; however, at any scan rate, the experimental capacity obtained from the microtubular electrode is greater than the capacity obtained at the control electrode. Figure 24 shows this effect more clearly as a plot of the ratio of the experimental capacities of the microtubular vs. control electrodes as a function of scan rate. At the highest scan rate employed, the microtubular electrode delivers almost seven times the experimental capacity of the control electrode, even though both electrodes contain the same amount of TiS_2.

These data show the third, and most significant, advantage of the microtubular current collector concept. The thinner TiS_2 films dispersed over the larger surface area insure that concentration polarization will be less of a problem at the this electrode relative to the control electrode.

Finally, Figure 25 shows the results of constant current discharge experiments at a microtubular electrode and a control electrode containing the same amount of TiS_2. Note that at this discharge current density, the microtubular electrode delivers 90% of its theoretical capacity. In contrast, the control electrode is suffering from concentration polarization and delivers significantly less capacity.

4. Conclusions. A new approach for preparing microstructured Li-ion battery electrodes was demonstrated. This approach entails using the template method to prepare a microtubular current collector and then doing CVD synthesis of the Li^+-intercalation material over this microstructured current collector. We have demonstrated that this microstructured electrode offers four advantages. First, because the surface area of the current collector is large, the thickness of the Li^+-intercalation material deposited over this microstructured current collector will be thin. This minimizes problems associated with unwanted voltage drop in the intercalation material. Second, the large surface area insures that the current density is low, and this minimizes problems associated with slow electron transfer kinetics. Third, the thinner films make the microstructured electrode less susceptible to concentration polarization. Fourth, in cases where the electronic conductivity of the intercalation material is low (e.g., the $LiMn_2O_4$ example discussed previously) the concentric tubular approach provides each particle of the intercalation material with its own internal current-collecting electrode.

ACKNOWLEDGMENTS

First, I would like to acknowledge the contributions of my professional colleagues, Professor Hiroshi Yoneyama of Osaka University and Professor Ellen R. Fisher of Colorado State University. Second, this work would not have been possible without the efforts of a talented group of post doctoral research associates and graduate students. These include, Dr. Vinod P. Menon, Dr. Ranjani V. Parthasarathy, Dr. Matsuhiko Nishizawa, Dr. Susumu Kuwabata, Mr. Kiyoshi Mukai, Dr. Guangli Che, Ms. Kshama B. Jirage, Ms. Brinda B. Lakshmi, and Dr. G. Louis Hornyak. The various aspects of this work have been supported by the Department of Energy, Office of Energy Research, Grant DE-FG03-95ER14576 (joint grant with Prof. Fisher), the Office of Naval Research and the National Science Foundation. Collaboration between CRM and Prof. Yoneyama was made possible by Grant-in-Aid for International Scientific Research Program: Joint Research, No. 0744150, from the Ministry of Education, Science, Culture, and Sports, Japan.

References

1. R. T. Bate, Sci. Am., 258: 96 (1988).
2. Science (special issue on nanomaterials), 254: 1300 (1991).
3. C. R. Martin, Science, 266: 1961 (1994).
4. C. R. Martin, Chem. Mater., 8: 1739 (1996).
5. C. R. Martin, Acc. Chem. Res., 28: 61 (1995).
6. J. C. Hulteen, and C. R. Martin, J. Mater. Chem., in press.
7. E. A. Medcalf, D. J. Newman, E. G. Gorman, and C. P. Price, Clin. Chem., 36: 446 (1990).
8. J. M. Simo, J. Joven, X. Cliville, and T. Sans, Clin. Chem., 40: 625 (1994).
9. L. B. Bangs, J. Clin. Immunoassay, 13: 127 (1990).
10. L. B. Bangs, Pure Appl. Chem., 68: 1873 (1996).
11. G. A. Ozin, Adv. Mater., 4: 612 (1992).
12. R. Gref, Y. Minamitake, M. T. Peracchia, V. Trubetskoy, V. Torchilin, and R. Langer, Science, 263: 1600 (1994).
13. R. Parthasarathy, and C. R. Martin, J. Appl. Poly. Sci., 62: 875 (1996).
14. C.-G. Wu, and T. Bein, Science, 264: 1757 (1994).
15. V. P. Menon, and C. R. Martin, Anal. Chem., 67: 1920 (1995).
16. R. M. Penner and C.R. Martin, Anal. Chem., 59: 2625 (1987).
17. I. F. Cheng, L. D. Whiteley, and C. R. Martin, Anal. Chem., 61: 762 (1989).
18. J. C. Hulteen, V. P. Menon, and C. R. Martin, J. Chem. Soc. Far. Trans. 1, 92: 4029 (1996).
19. M. Nishizawa, V. P. Menon, and C.R. Martin, Science, 268: 700 (1995).
20. C. A. Foss, G. L. Hornyak, J. A. Stockert, and C. R. Martin, J. Phys. Chem., 98: 2963 (1994).
21. G. L. Hornyak, C. J. Patrissi, and C. R. Martin, J. Phys. Chem. B, 101: 1548 (1997).

22. H. C. Van de Hulst, Light Scattering by Small Particles. Dover Publications, Inc, NY, p. 397 (1981).

23. K. R. Wehmeyer, and R. M. Wightman, J. Electroanal. Chem., 196: 417 (1985).

24. R. M. Penner, M. J. Heben, T. L. Longin, and N. S. Lewis, Science, 250: 1118 (1990).

25. E. Sabatani, and I. Rubinstein, J. Phys. Chem., 91: 6663 (1987).

26. R. Bilewicz, and M. Majda, J. Am. Chem. Soc., 113: 5464 (1991).

27. R. S. Nicholson, Anal. Chem., 37: 1351 (1965).

28. C. Amatore, J. M. Savéant, and D. Tessier, J. Electroanal. Chem., 147: 39 (1983).

29. B. Ballarin, C. J. Brumlik, D. R. Lawson, W. Liang, L. S. Van Dyke, and C. R. Martin, Anal. Chem., 64: 2647 (1992).

30. V. P. Menon, Ph.D. Dissertation, Colorado State University (1996).

31. H. S. White, A. J. Bard, and F.-R. Fan, Personal communication, July, 1994.

32. R. L. Dotson, and K. E. Woodard, Perfluorinated Ionomer Membranes, (A. Eisenberg and H.L. Yeager, Eds.) Vol. 180 of the ACS Symposium Series, American Chemical Society, Washington DC (1982).

33. J. Koryta, Ion-Selective Electrodes, Cambridge Univ. Press, Cambridge, pp. 21-23 (1975).

34. A. J. Bard, and L. R. Faulkner, Electrochemical Methods, Wiley, New York, pp. 500-515 (1980)

35. See W. J. Petzny, and J. A. Quinn, Science, 166: 751 (1969). C. Liu, Ph.D. Dissertation, Texas A & M University, (College Station, TX, 1991).

36. N. Lakshminarayanaiah, Transport Phenomena in Membranes, Academic Press, New York, Chap. 3 (1969).

37. S. Biggs, P. Mulvaney, C. F. Zukoski, and F. Grieser, J. Am. Chem. Soc., 116: 9150, (1994).

38. C. Liu, and Martin, J. Electrochem. Soc., 137: 3114 (1990).

39. D. L. Rath, and W. N. Hansen, Surf. Sci., 136: 195 (1984).

40. In fact, at the pzc, the membrane should show the liquid junction potential (36) based on the transference numbers of the ions in the bulk solution.

41. J. Clavilier, and C.N.V. Huong, J. Electroanal. Chem., 80: 101 (1977). This reported pzc is for polycrystalline Au. Electrochemists may debate the precise meaning of the pzc for a polycrystalline metal surface. However, for the purposes of this paper, it is the potential at which there is no net excess charge on the polycrystalline metal surface.

42. M. R. Deakin, T. T. Li, and O.R. Melroy, J. Electroanal. Chem., 243: 343 (1988).

43. A. Ulman, A. An Introduction to Ultrathin Organic Films from Langmuir-Blodgett to Self-Assembly, Academic Press, San Diego (1991).

44. This is undoubtedly because prior studies have shown that because of its short alkyl chain, PT monolayers are disordered. See C. D. Bain, E. B. Troughton, Y.-T. Tao, J. Evall, G. M. Whitesides, and R. G. Nuzzo, J. Am. Chem. Soc., 111: 321 (1989).

45. Although polymeric membranes that show switchable transport properties have been described (see, for example, P. Burgmayer, and R. W. Murray, J. Phys. Chem., 88: 2515 (1984)) the switchability was based on Faradaic electrolysis of the polymer.

46. C. R. Martin, D. T. Mitchell, and J. C. Hulteen, Anal. Chem., Submitted.

47. D. Linden, Handbook of Batteries (2nd). New York, P36.24 (1995).

48. S. Megahed, and B. Scrosati, J. Power Sources, 51: 79 (1994).

49. A. L. Tipton, S. Passerini, B.B. Owens, and W. H. Smyrl, J. Electrochem. Soc., 143:3473 (1996).

50. T. D. Tran, J. H. Feikert, R. W. Pekala, and K. Kinoshita, J. Applied Electrochem., 26: 1161 (1996).

51. J. J. Auborn, and Y. L. Barberio, J. Electrochem. Soc., 134: 638 (1987).

52. T. F. Fuller, M. Doyle, and J. Newman, J. Electrochem. Soc., 141: 1 (1994).

53. M. Doyle, T. F. Fuller, and J. Newman, J. Electrochem. Soc., 140: 1526 (1993).

54. M. S. Whittingham, Prog. Solid. St. Chem., 12: 41 (1978).

55. M. Nishizawa, K. Mukai, S. Kuwabata, C. R. Martin, and H. Yoneyama, J. Electrochem. Soc., In press.

56. A. H. Gemeay, H. Nishiyama, S. Kuwabata, and H. Yoneyama, J. Electrochem. Soc., 142: 4190 (1995).

57. M.M. Thackeray, J. Electrochem. Soc., 142: 2558 (1995).

58. V. M. Cepak, J. C. Hulteen, G. Che, K. B. Jirage, B. B. Lakshmi, E. R. Fisher, and C. R. Martin, Chem. Mater., 9: 1065 (1997).

59. G. Che., K. B. Jirage, E. R. Fisher, and C. R. Martin, J. Electrochem. Soc., Submitted.

60. J. R. Bottin, P. R. McCurdy, and E. R. Fisher, Rev. Sci. Instrum. In press.

61. B. V. Ratnakumar, G. Nagasubramanian, S. D. Stefano, and C. P. Bankston, J. Electrochem. Soc., 139: 1531 (1992).

62. E. Laviron, J. Electroanal. Chem., 52: 395 (1974).

Table I. Characteristics of the membranes.

Pore diameter (nm)	Pore density (cm^{-2})	Distance between pores (μm)	Fractional pore area[a]	Fractional electrode area[b]
10	$6x10^8$	0.2	0.00047	0.00094
30	$6x10^8$	0.2	0.0042	0.0042

[a] Determined from electron micrographs of membrane.

[b] Determined electrochemically.

Figure Captions

1. Electron micrographs of polycarbonate (**A** and **B**) and alumina (**C** and **D**) template membranes. For each type of membrane, an image of a larger pore membrane is presented (**A** and **C**) so that the characteristics of the pores can be clearly seen. An image of a membrane with nanopores is also presented (**B** and **D**). **A.** Scanning electron micrograph of the surface of a polycarbonate membrane with 1 μm-diameter pores. **B.** Transmission electron micrograph (TEM) of a graphite replica of the surface of a polycarbonate membrane with 30 nm-diameter pores. The pores appear "ragged." This is an artifact of the graphite replica. **C** and **D.** TEMs of microtomed sections of alumina membranes with 70 nm (**C**) and ~10 nm (**D**) diameter pores.

2. **A.** Scanning electron micrograph of an array of gold nanotubules protruding from a substrate surface. **B.** Transmission electron micrograph of three polypyrrole nanotubules.

3. Transmission electron micrograph of a microtomed section of a polycarbonate template membrane after deposition of Au tubules within the pores of the membrane. Pore diameter was 50-nm.

4. UV-Visible spectra of a 30NEE and a 10NEE.

5. Cyclic voltammograms at 100 mV s^{-1} at a 10NEE in 5 μM aqueous $TMAFc^+$, 1 mM $NaNO_3$ **A.** Before thermal treatment and **B.** After thermal treatment of the NEE.

6. Background cyclic voltammograms in 50 mM $NaNO_3$ at 100 mV s^{-1} for **A.** Gold macro-disk electrode. **B.** 30NEE. **C.** 10NEE. The geometric area for all electrodes was 0.079 cm^2.

7. Simulated (dotted curves) and experimental (solid curves) voltammograms at 100 mV s^{-1} at a 10NEE (0.079 cm^2 geometric area) in 5 μM

$TMAFc^+$ and 0.5 mM sodium nitrate. Simulation assumes the total overlap limiting case (i.e., a macro-electrode with area = 0.079 cm^2).

8. Cyclic voltammograms for 5 µM $Ru(NH_3)_6Cl_3$ and 10 mM pH 7 phosphate buffer as supporting electrolyte. **A.** 30NEE. **B.** 10NEE. Scan rates are 20, 50 and 100 mV s^{-1}.

9. Cyclic voltammograms at 100 mV s^{-1} in aqueous $TMAFc^+$ at **A.** A gold macro-disk electrode in 50 mM sodium nitrate. **B.** A 10NEE in 1 mM sodium nitrate. $TMAFc^+$ concentrations are as indicated; electrode geometric area in both cases=0.079 cm^2.

10. Cyclic voltammograms illustrating the effect of supporting electrolyte concentration at a 10NEE. 5 µM $TMAFc^+$ in aqueous $NaNO_3$ at the indicated concentrations of $NaNO_3$. Scan rate = 100 mV s^{-1}.

11. E_m values obtained for membranes prepared for the indicated plating times. The solution on the l side of the membrane was 0.1 mM KCl. The solution on the h side of the membrane was varied from 0.1 mM KCl to 1 M KCl. The E_m values were measured by using two Ag/AgCl (KCl saturated) electrodes placed in each half-cell through agar salt-bridges. The dashed line is for ideal cation-permselective behavior.

12. Variation of E_m with potential applied to the membrane (1 mM KF on the l side, and 10 mM KF on the h side, of the membrane; tubule radius ~1.1 nm). The potential of the membrane was controlled with a potentiostat verses a Ag/AgCl reference electrode immersed in the side-h solution.

13. Variation of E_m with potential applied to the membrane (1 mM KBr on l side and 10 mM KBr on h side; membrane as per Fig. 12) for an untreated Au nanotubule membrane (upper curve) and a PT-coated membrane (lower curve).

14. Schematic of the procedure used to prepare the $LiMn_2O_4$ tubules.

15. Scanning electron micrograph of the $LiMn_2O_4$ tubules.

16. Charge discharge curves for nanotubular (a) and thin film (b) $LiMn_2O_4$/polypyrrole electrodes. Current density = 0.1 mA cm^{-2}. Electrolyte was 1 M $LiClO_4$ in 1:1 (vol) propylene carbonate:dimethoxyethane.

17. Ratio of the specific capacities of the thin film and tubular electrodes.

18. Schematic diagram of the fabrication of the Au/TiS_2 concentric tubular electrode.

19. Scanning electron micrographs. **A.** The template-synthesized gold tubule ensemble obtained after dissolution of the polyester template membrane. **B.** As per A but after CVD synthesis of TiS_2 outer tubes on the Au inner tubes. These tubular microstructures contained 0.86 mg of TiS_2 cm^{-2} of substrate Al surface area. **C.** As per B but with a larger quantity (2.04 mg cm^{-2}) of TiS_2. **D.** CVD TiS_2 film.

20. Lithium intercalation and deintercalation cyclic voltammograms for thicker control TiS_2 film (2.13 mg TiS_2 cm^{-2}) electrode **(a,a')** and microtubular (2.04 mg TiS_2 cm^{-2}) **(b,b')** electrode. Scan rates: (a,b) = 0.5 mV s^{-1} and (a',b') = 0.1 mV s^{-1}.

21. Lithium intercalation and deintercalation cyclic voltammograms for thinner film control TiS_2 electrode (0.60 mg TiS_2 cm^{-2}) **(a,a')** and microtubular electrode (0.86 mg TiS_2 cm^{-2}) **(b,b')**. Scan rates: (a,b) = 0.5 mV s^{-1} and (a',b') = 0.1 mV s^{-1}.

22. Cyclic voltammograms for a TiS_2 microtubular electrode. **A.** With increasing amounts of positive feedback. Scan rate = 1 mV s^{-1}. The level of applied positive feedback increased from **a** (none applied) to **c** (maximum applied). **B.** At a much lower scan rate (0.1 mV s^{-1}) and no applied feedback.

23. Discharge capacity vs. scan rate for **A.** TiS_2 microtubular electrode (2.04 mg cm^{-2}) and **B.** TiS_2 film control electrode (2.13 mg cm^{-2}).

24. Ratio of capacities (vs. scan rate) for the electrodes described in Figure 23.

25. Constant current (1 mA cm^{-2}) discharge curves. **A.** A microtubular electrode (1.5 mg TiS_2 cm^{-2}). **B.** A control electrode (1.3 mg TiS_2 cm^{-2}).

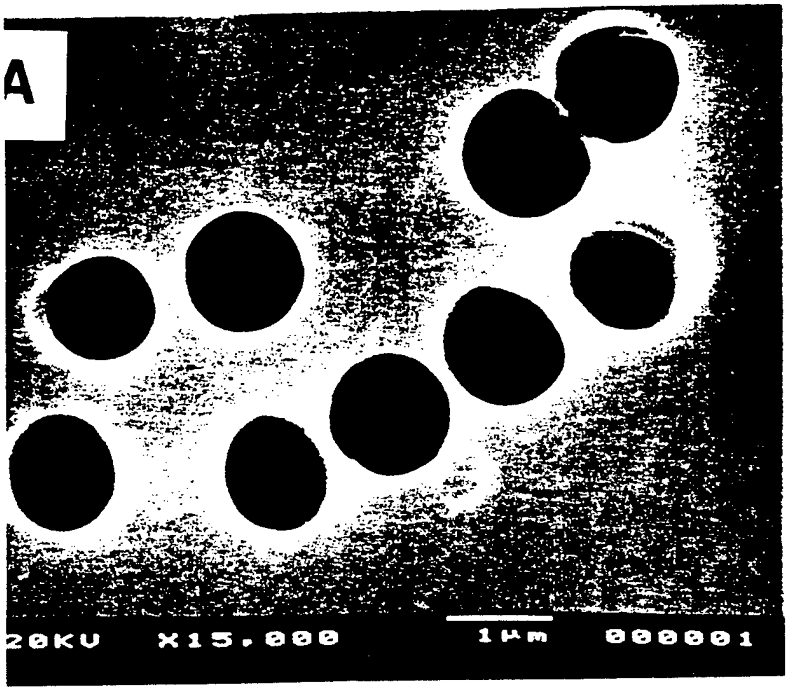
A
20KV X15,000 1μm 000001

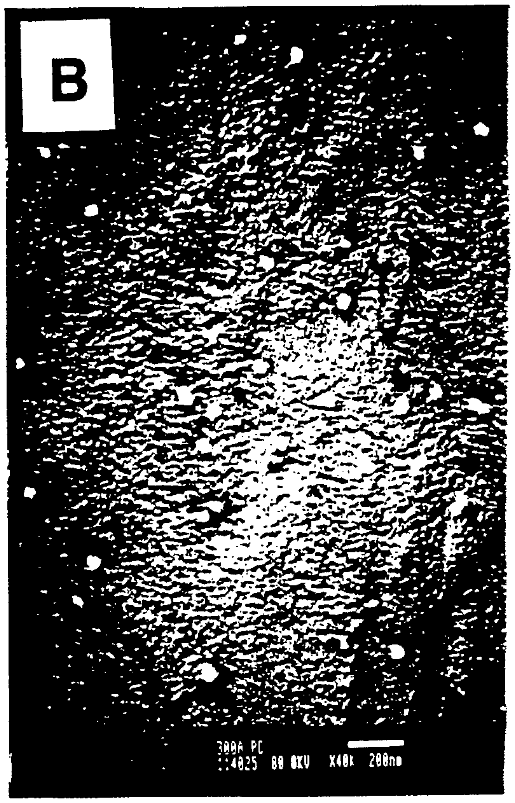
B
300A PC
114025 80.0KV X40k 200nm

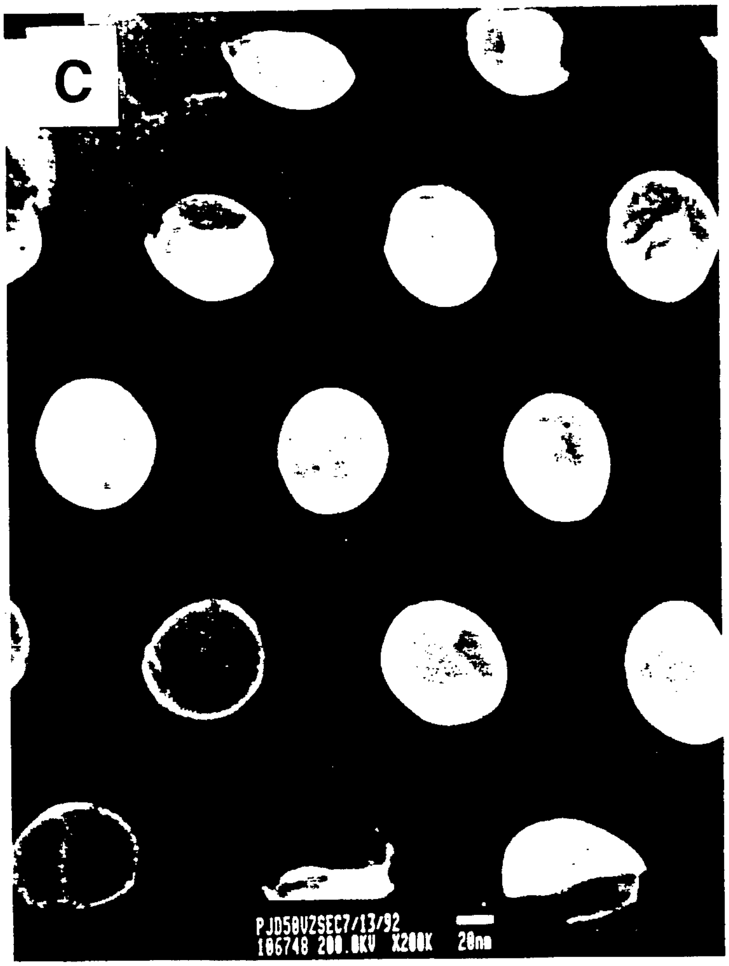
C
PJD50VZSEC7/13/92
106748 200.0KV X200K 20nm

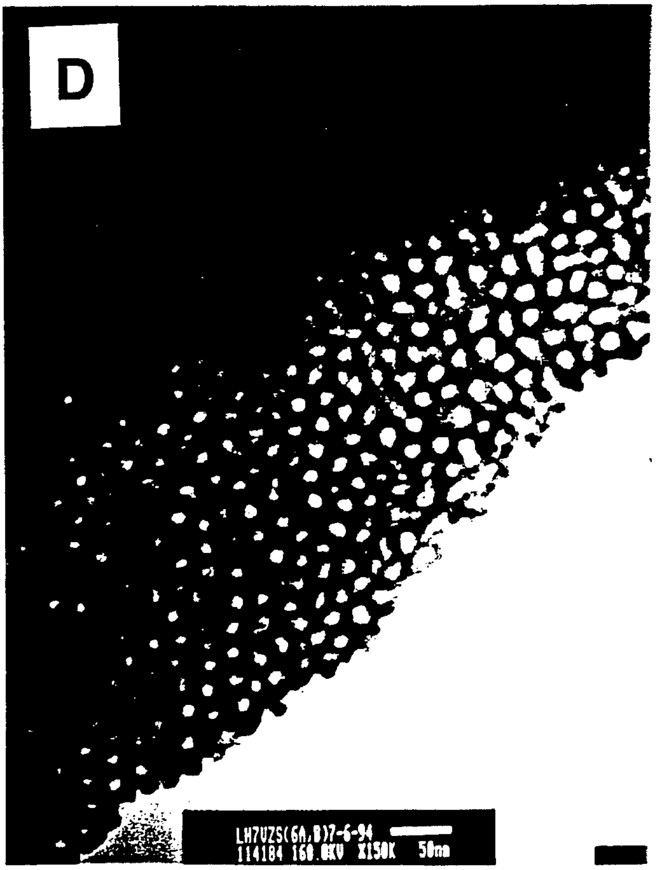
D
LH7UZS(6A,B)7-6-94
114184 160.0KV X150K 50nm

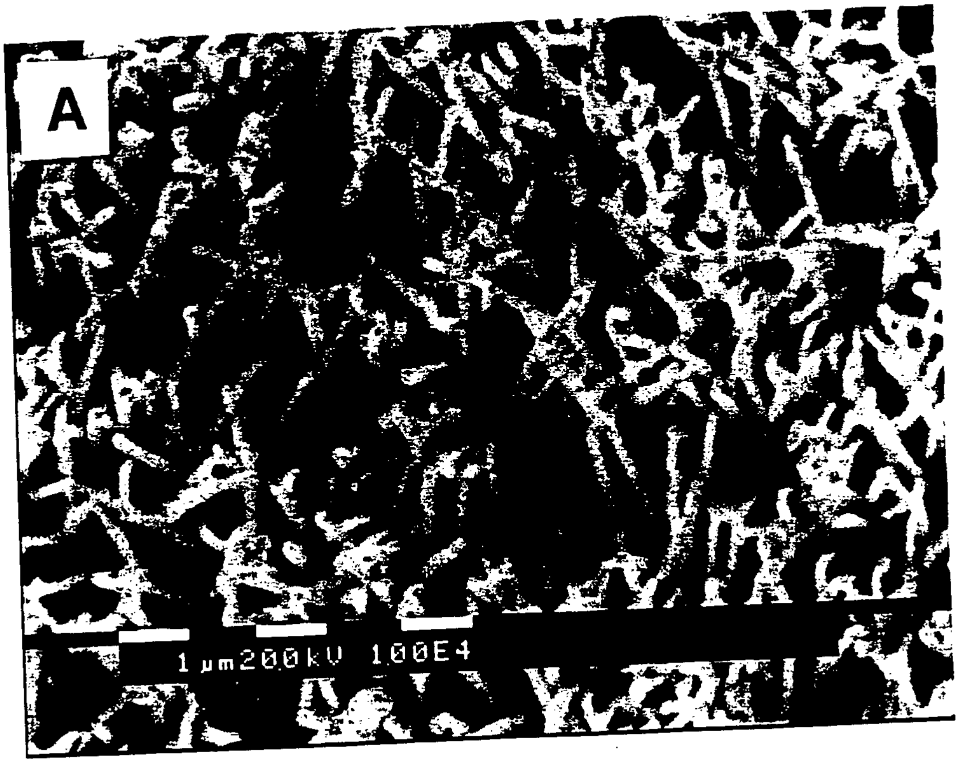
A
1 μm 200kV 100E4

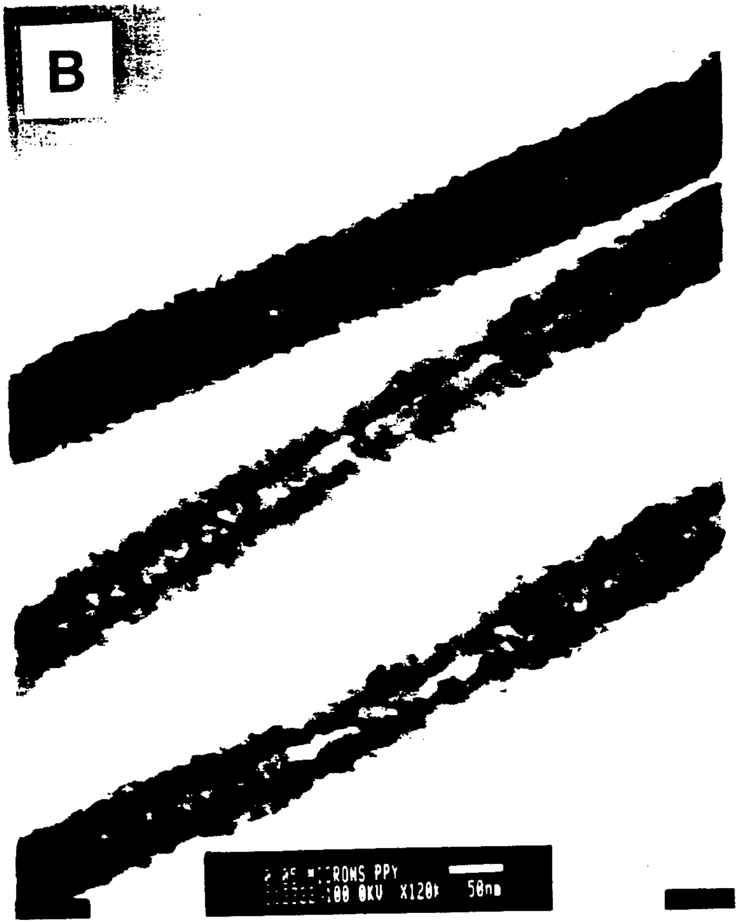
B
0.05 MICRONS PPY
100 0KV X120k 50nm

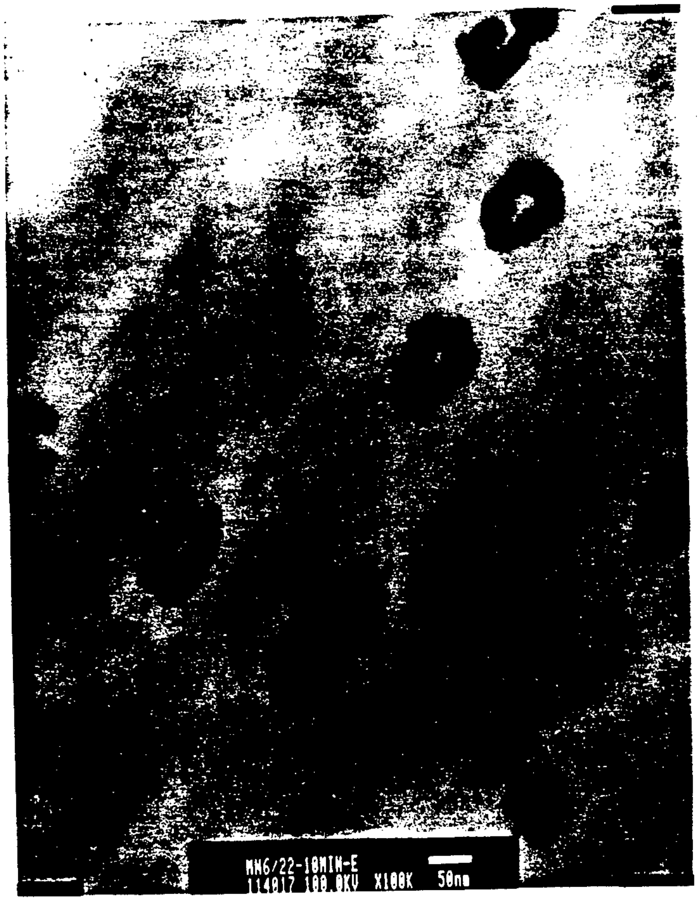
MN6/22-10MIN-E
114017 100.0KV X100K 50nm

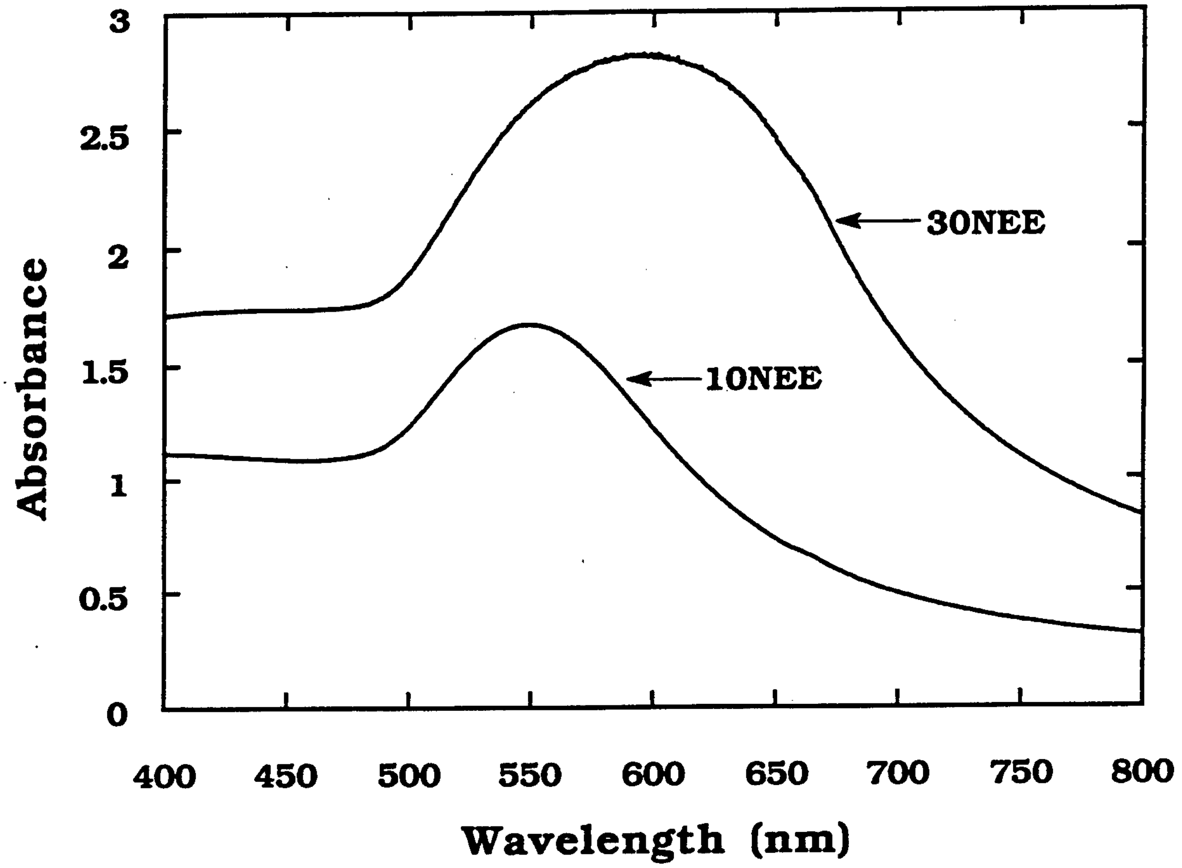

3
2.5
2
1.5
1
0.5
0
400
450
500
550
600
650
700
750
800
Absorbance
Wavelength (nm)
30NEE
10NEE

Fig 1

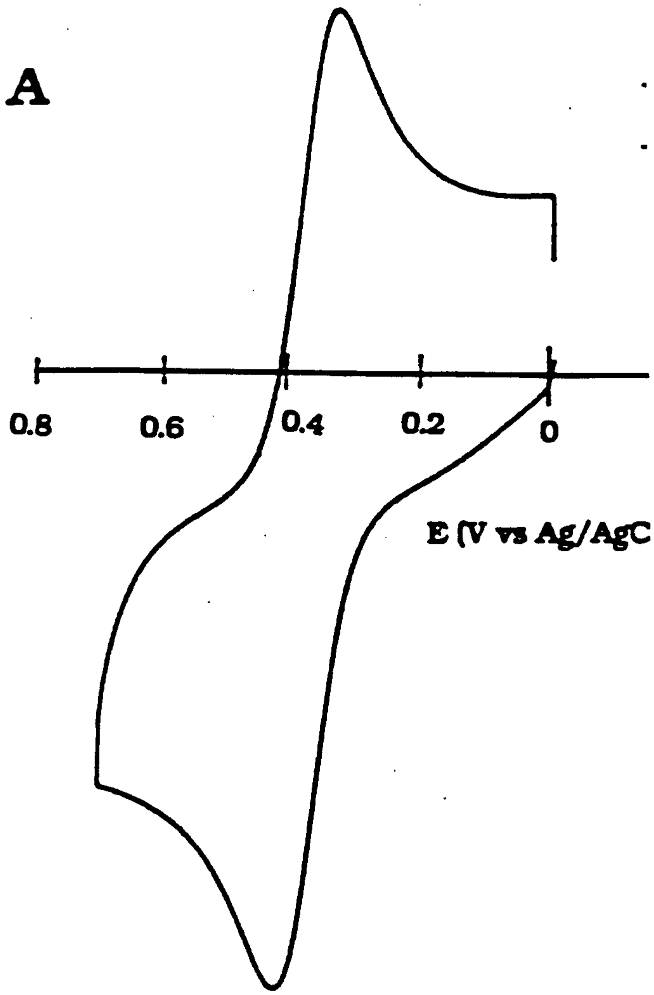

Fig 5A

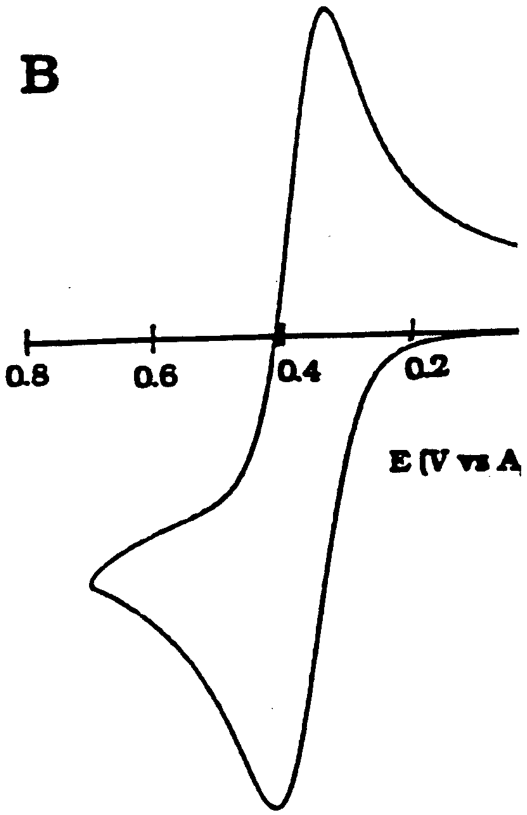

Fig 5B

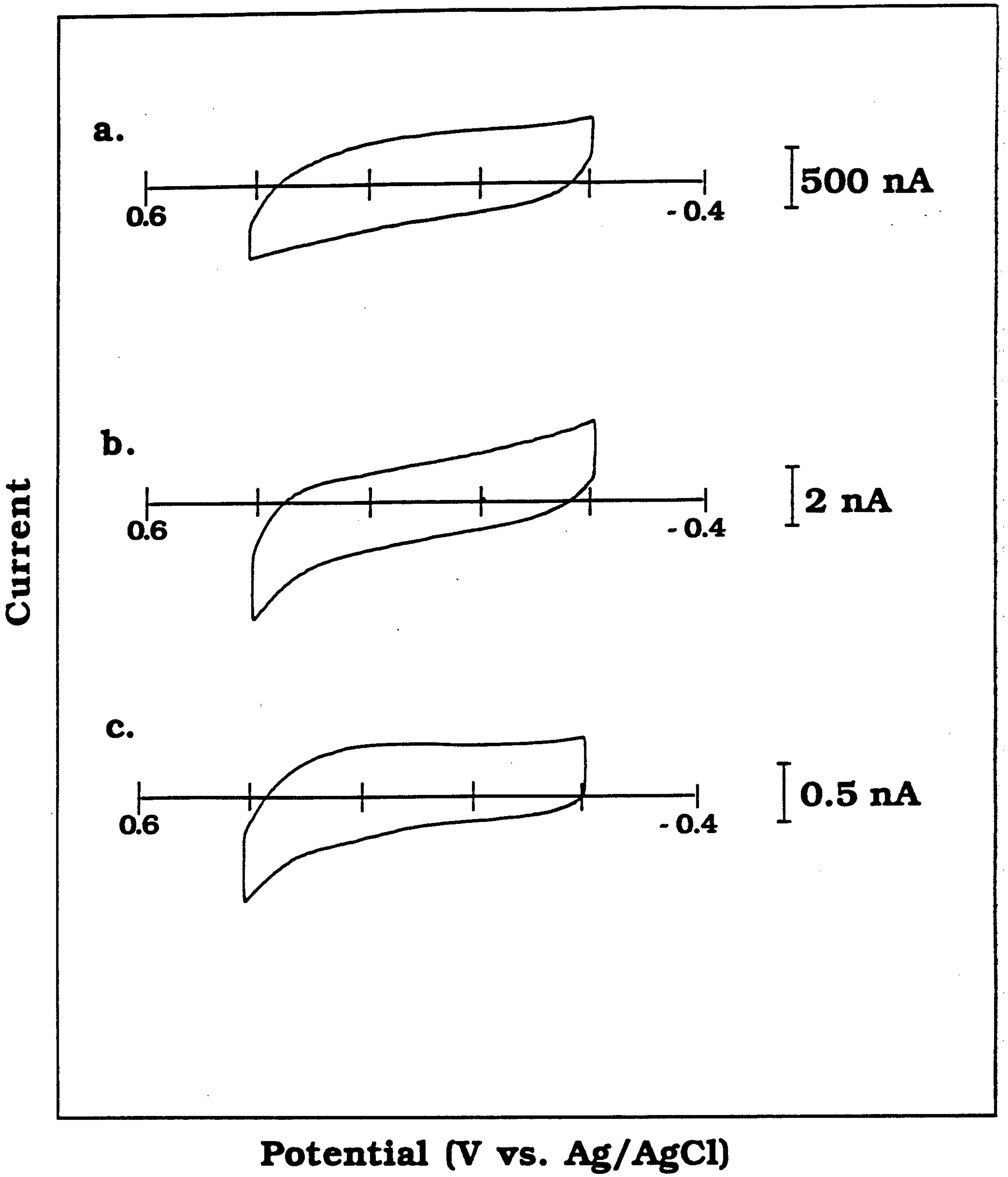
a.
0.6
- 0.4
500 nA
b.
0.6
- 0.4
2 nA
c.
0.6
- 0.4
0.5 nA
Current
Potential (V vs. Ag/AgCl)

Fig 6

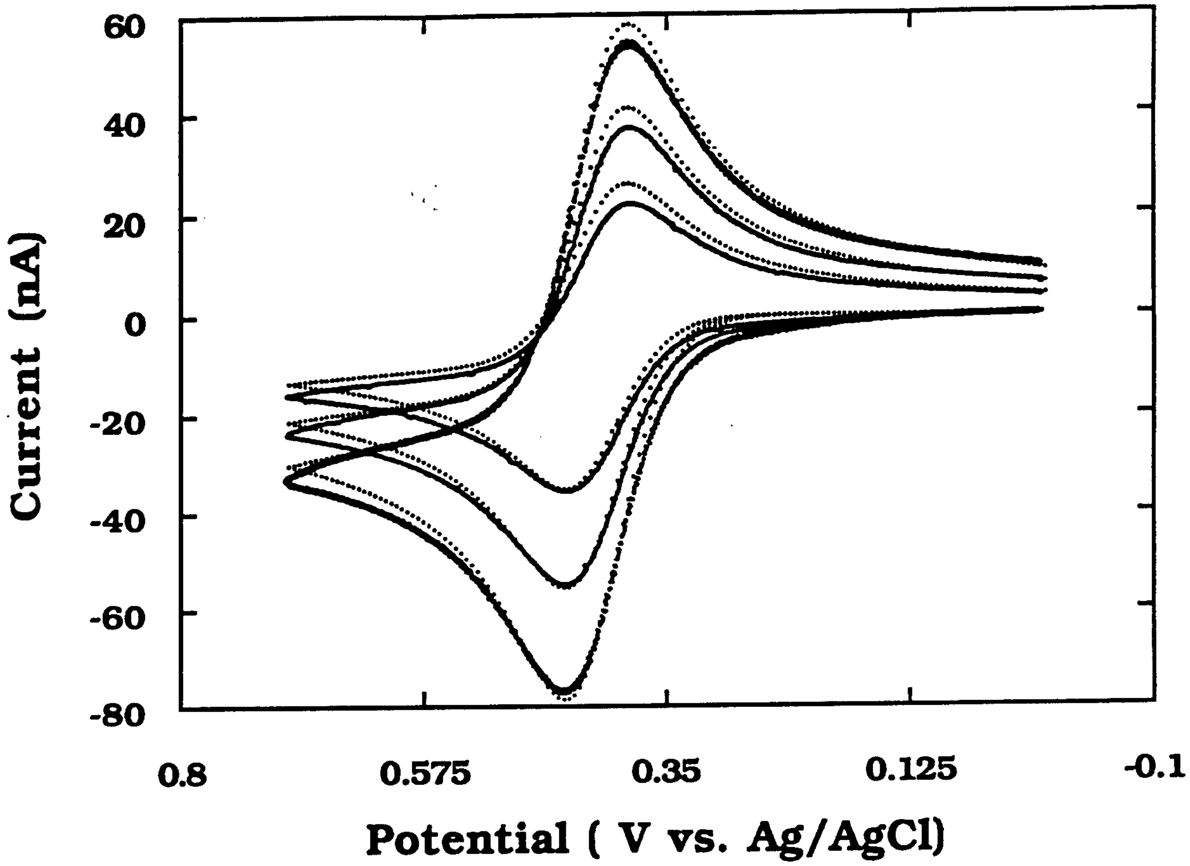
60
40
20
0
-20
-40
-60
-80
Current (nA)
0.8
0.575
0.35
0.125
-0.1
Potential (V vs. Ag/AgCl)

Fig 7

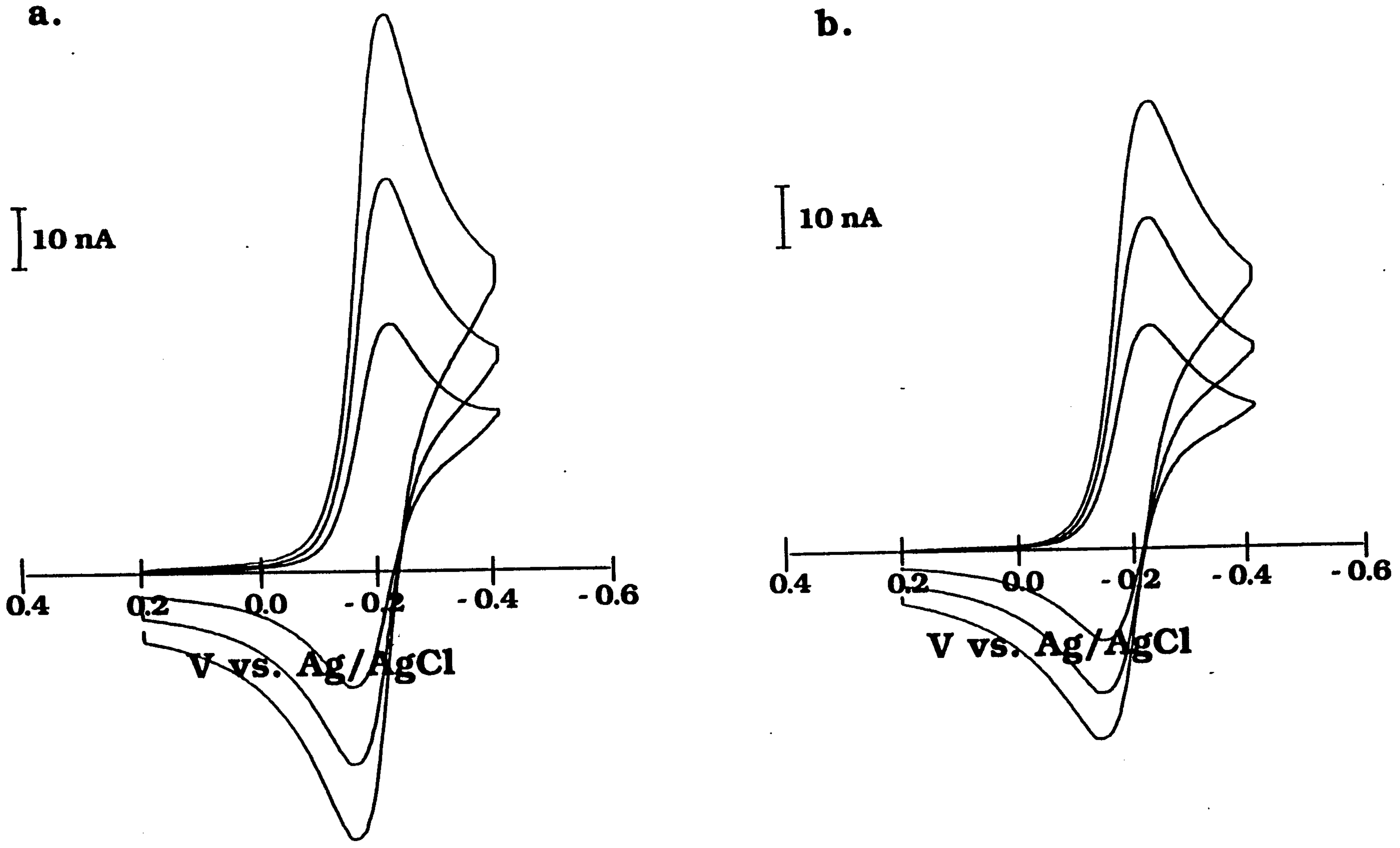
a.
10 nA
0.4
0.2
0.0
- 0.2
- 0.4
- 0.6
V vs. Ag/AgCl
b.
10 nA
0.4
0.2
0.0
- 0.2
- 0.4
- 0.6
V vs. Ag/AgCl

Fig 8

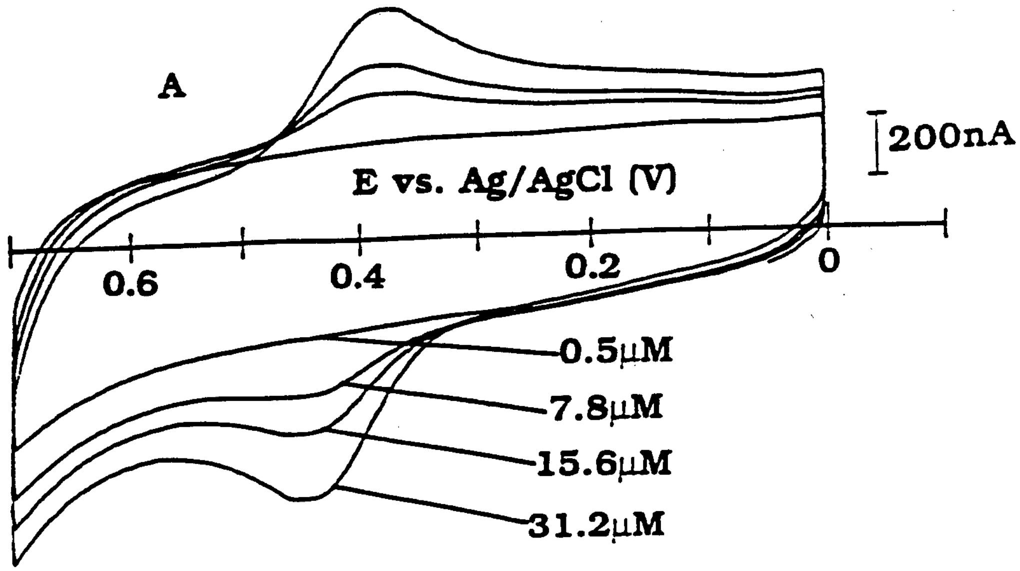

Fig 9A

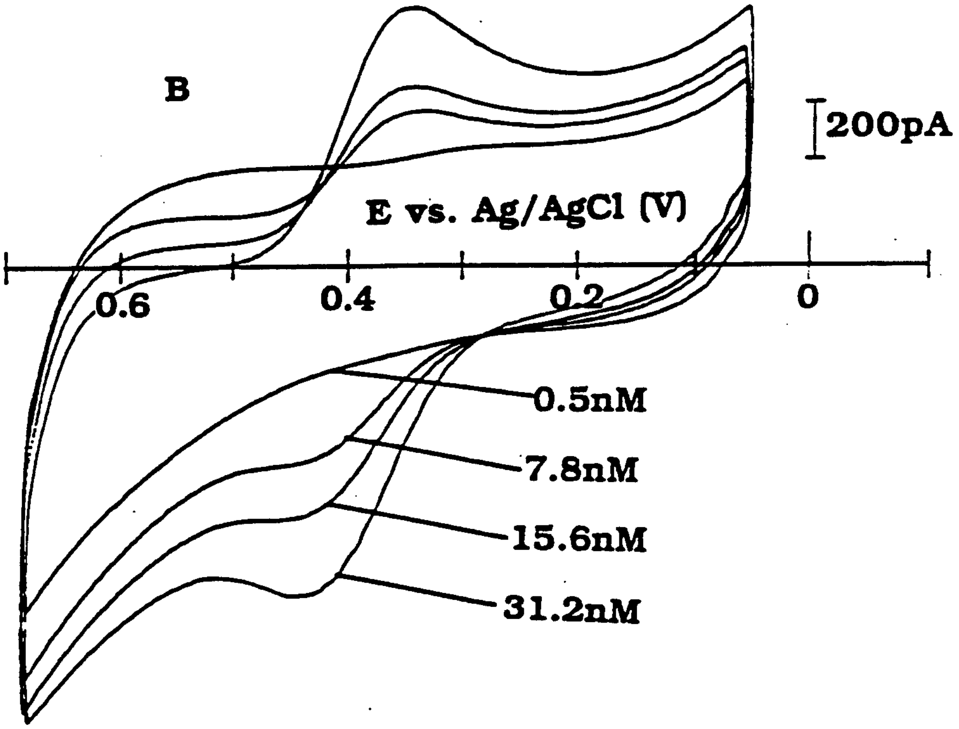

Fig 9B

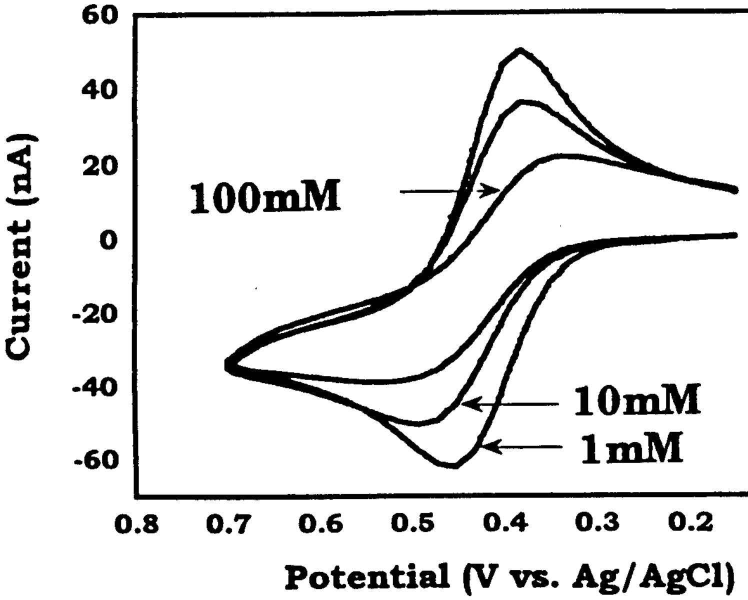
60
40
20
0
-20
-40
-60
Current (nA)
0.8
0.7
0.6
0.5
0.4
0.3
0.2
0.1
0
Potential (V vs. Ag/AgCl)
100mM
10mM
1mM

Fig. 5

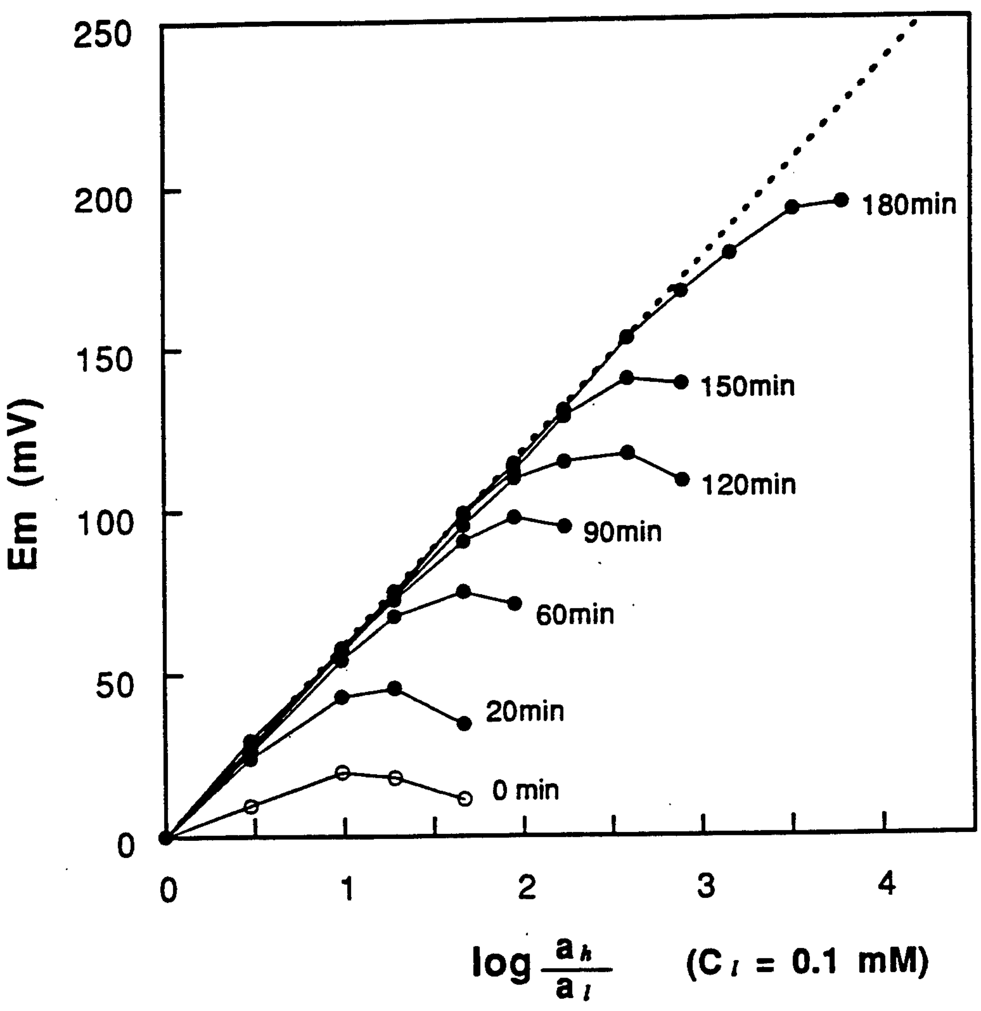
250
200
150
100
50
0
Em (mV)
0
1
2
3
4
$\log \frac{a_h}{a_l}$ (C_l = 0.1 mM)
180min
150min
120min
90min
60min
20min
0 min

Fig.1

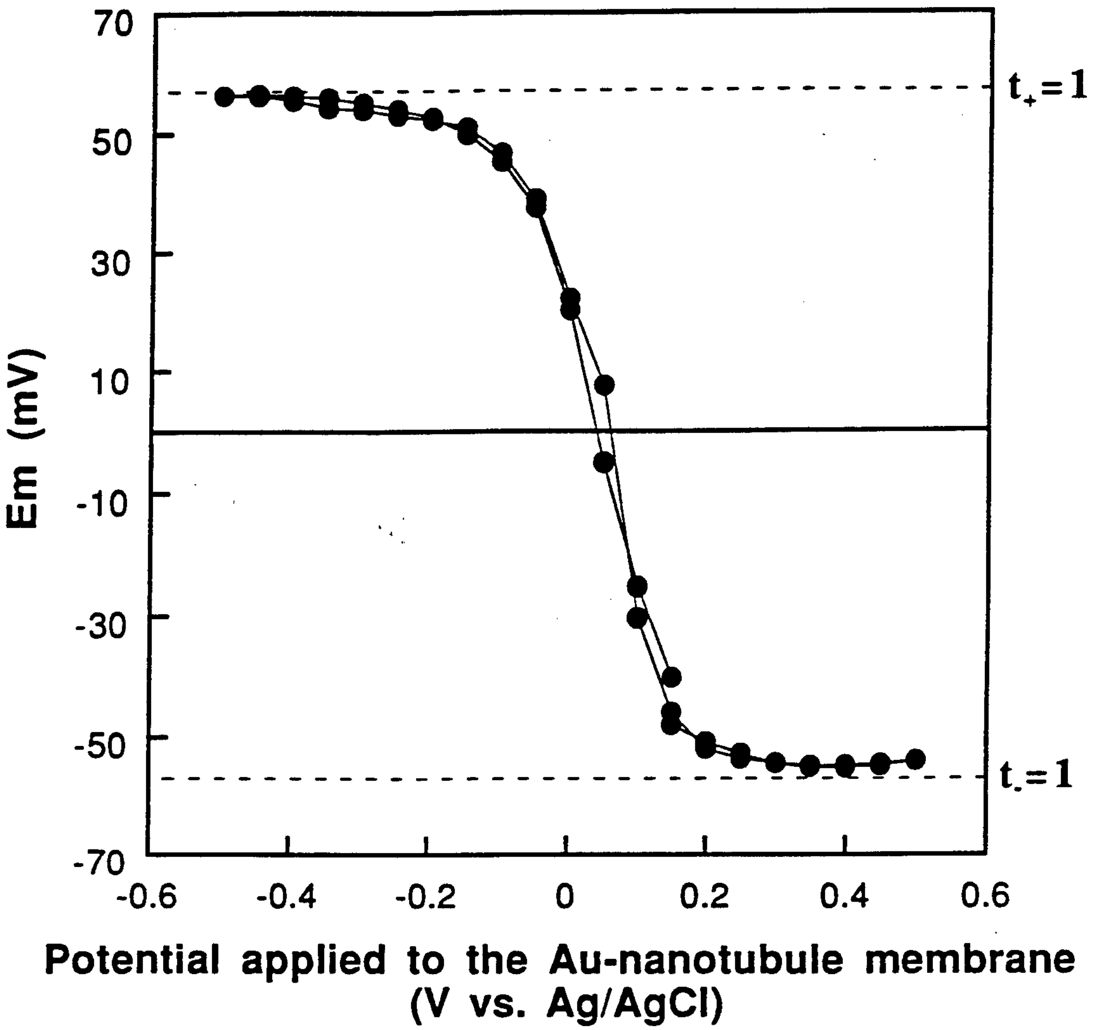
70
50
30
10
-10
-30
-50
-70
Em (mV)
t₊=1
t₋=1
-0.6
-0.4
-0.2
0
0.2
0.4
0.6
Potential applied to the Au-nanotubule membrane
(V vs. Ag/AgCl)

F. 2

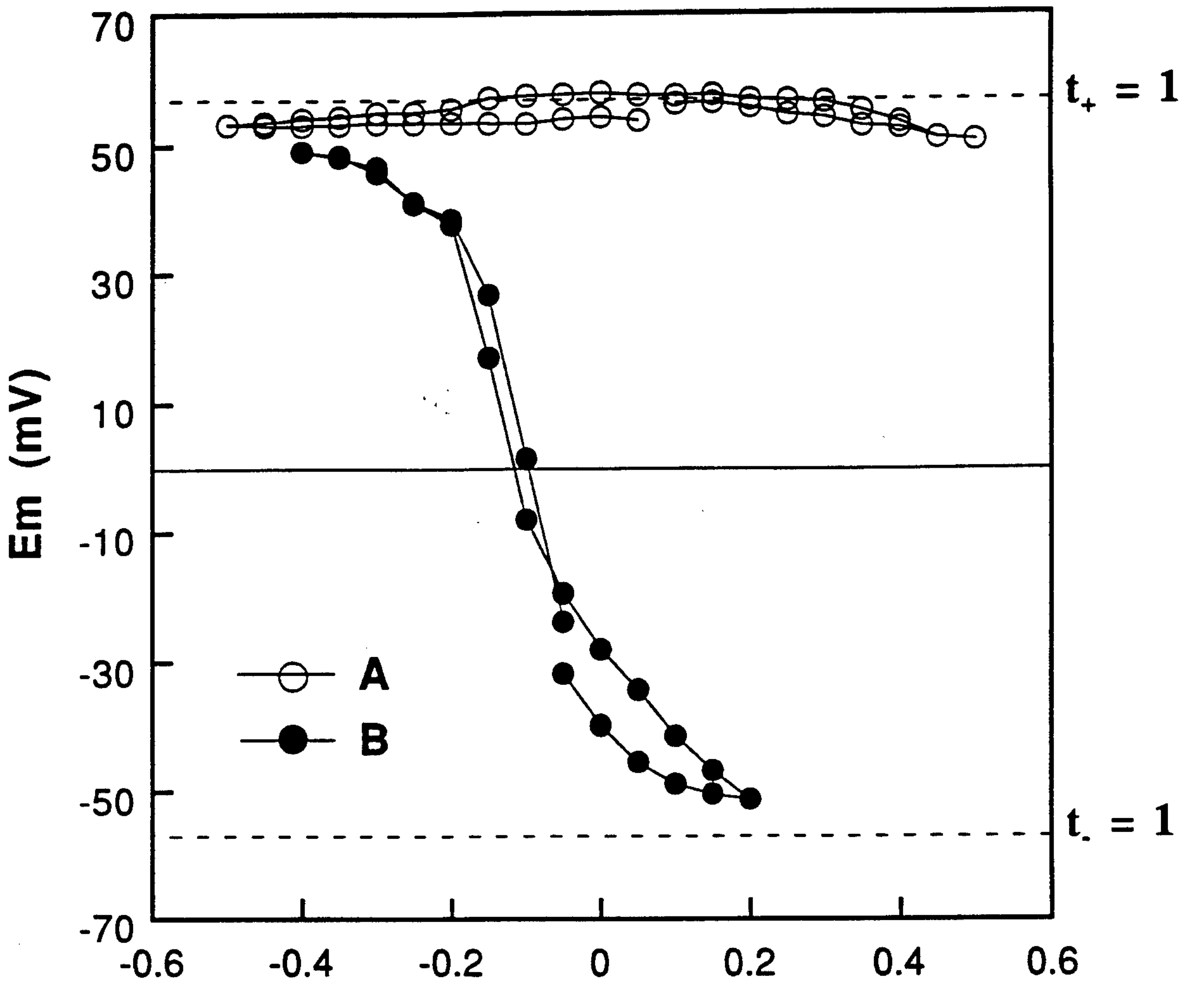
70
50
30
10
-10
-30
-50
-70
Em (mV)
-0.6
-0.4
-0.2
0
0.2
0.4
0.6
$t_+ = 1$
$t_- = 1$
A
B

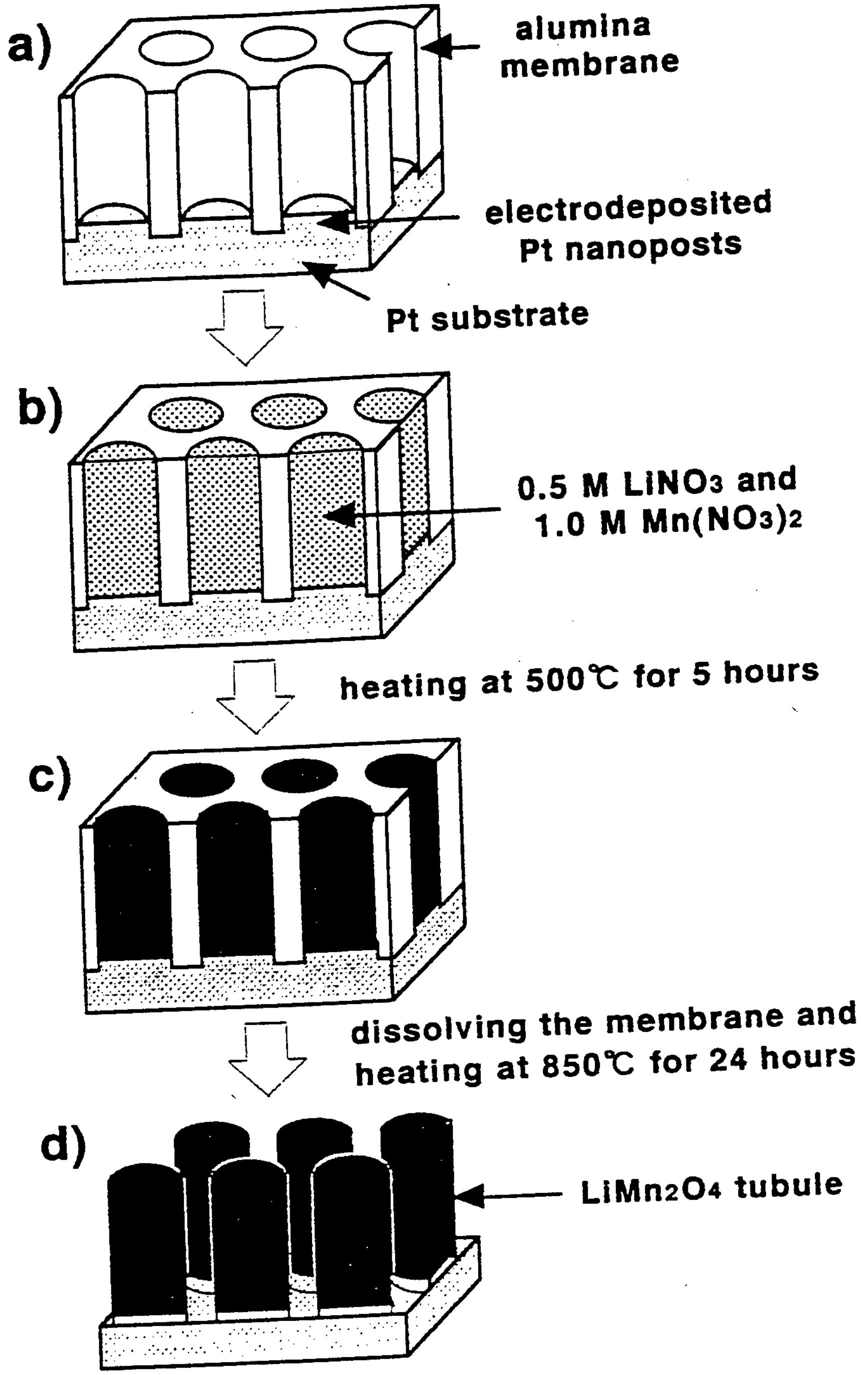
a)
alumina membrane
electrodeposited Pt nanoposts
Pt substrate
b)
0.5 M LiNO3 and 1.0 M Mn(NO3)2
heating at 500℃ for 5 hours
c)
dissolving the membrane and heating at 850℃ for 24 hours
d)
LiMn2O4 tubule

Fig 14

012502 20KV X50.0K 0.60um

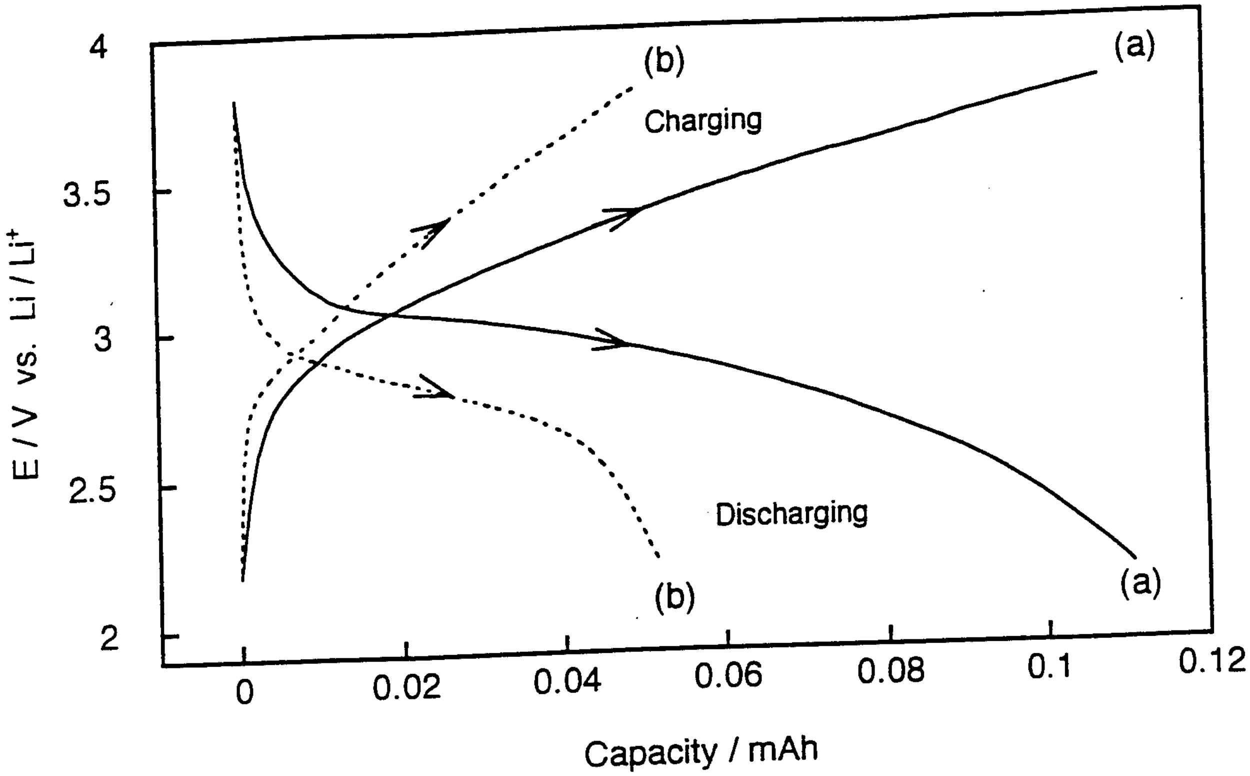
4
3.5
3
2.5
2
E / V vs. Li / Li$^+$
0
0.02
0.04
0.06
0.08
0.1
0.12
Capacity / mAh
(b)
(a)
Charging
Discharging
(b)
(a)

Fig. 5

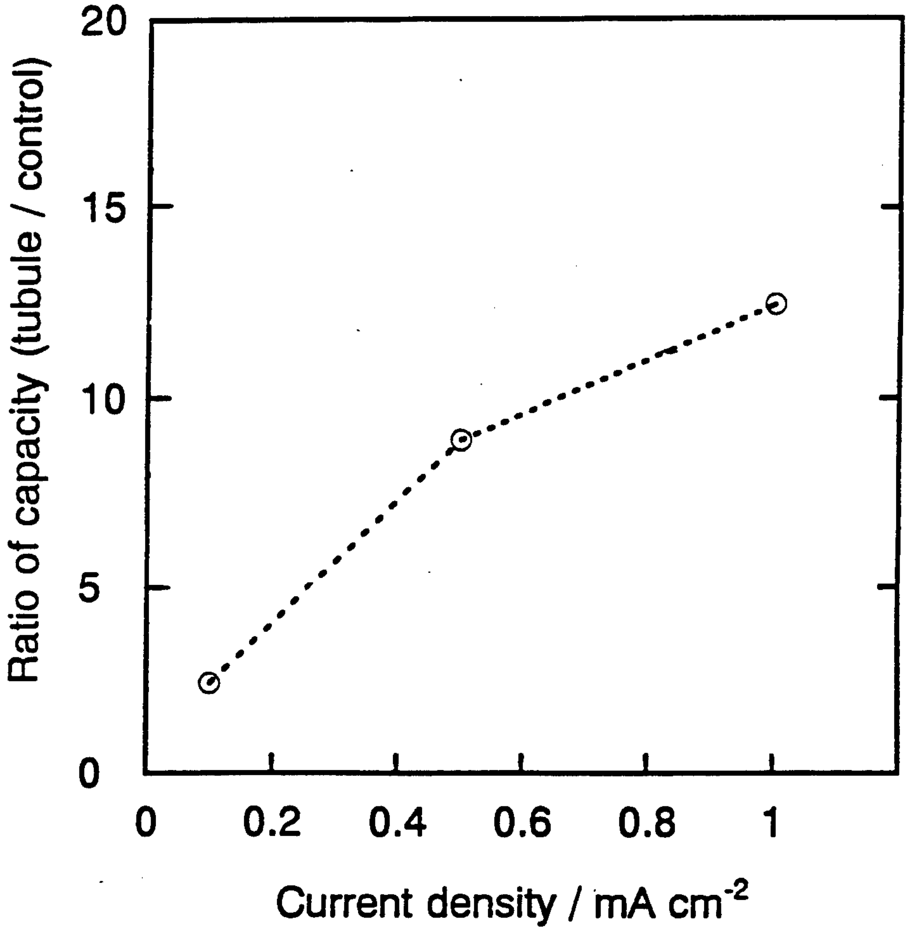
20
15
10
5
0
0
0.2
0.4
0.6
0.8
1
Ratio of capacity (tubule / control)
Current density / mA cm^{-2}

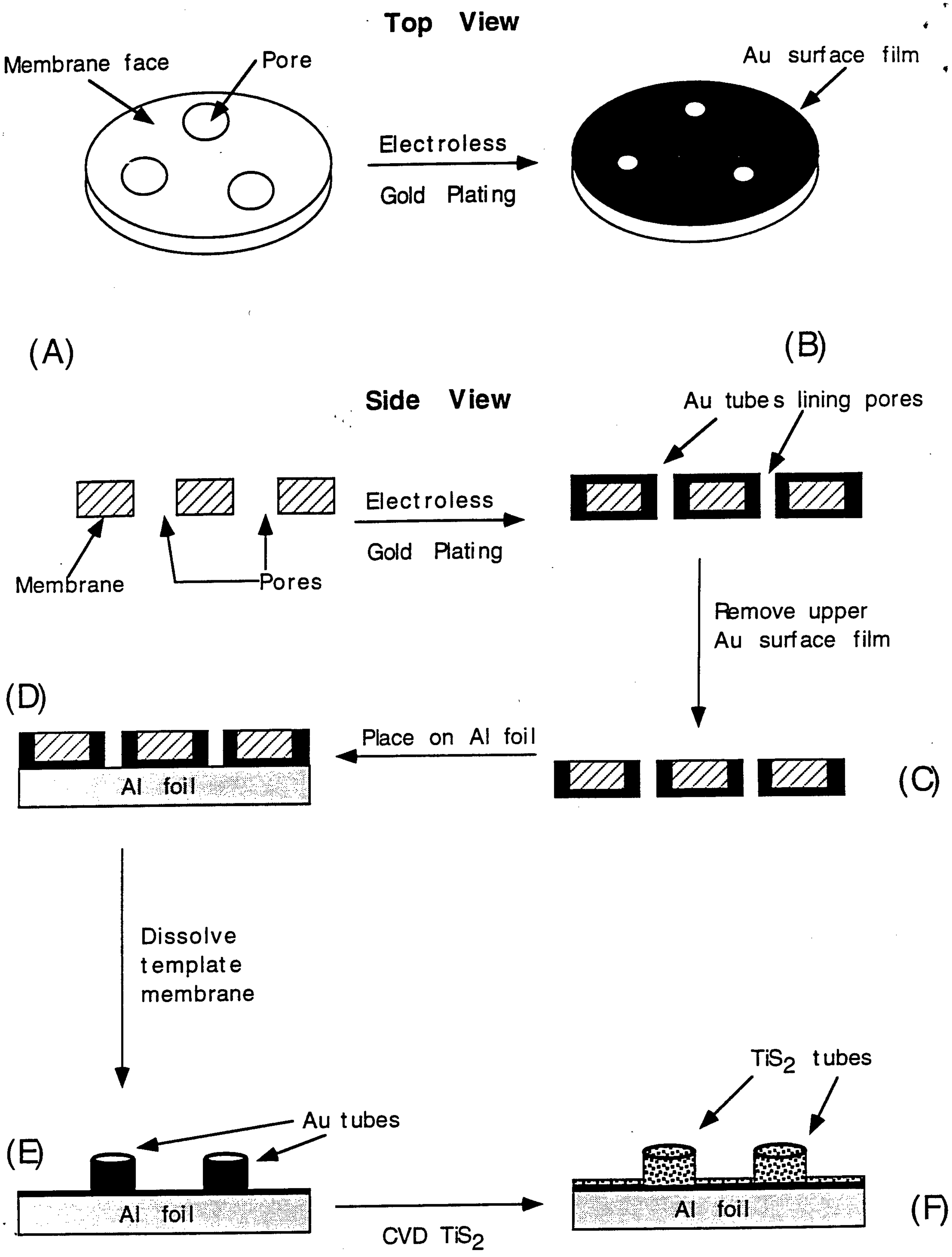
Top View
Membrane face
Pore
Electroless
Gold Plating
Au surface film
(A)
(B)
Side View
Au tubes lining pores
Membrane
Pores
Electroless
Gold Plating
Remove upper
Au surface film
(D)
Place on Al foil
Al foil
(C)
Dissolve
template
membrane
TiS_2 tubes
Au tubes
(E)
Al foil
CVD TiS_2
Al foil
(F)

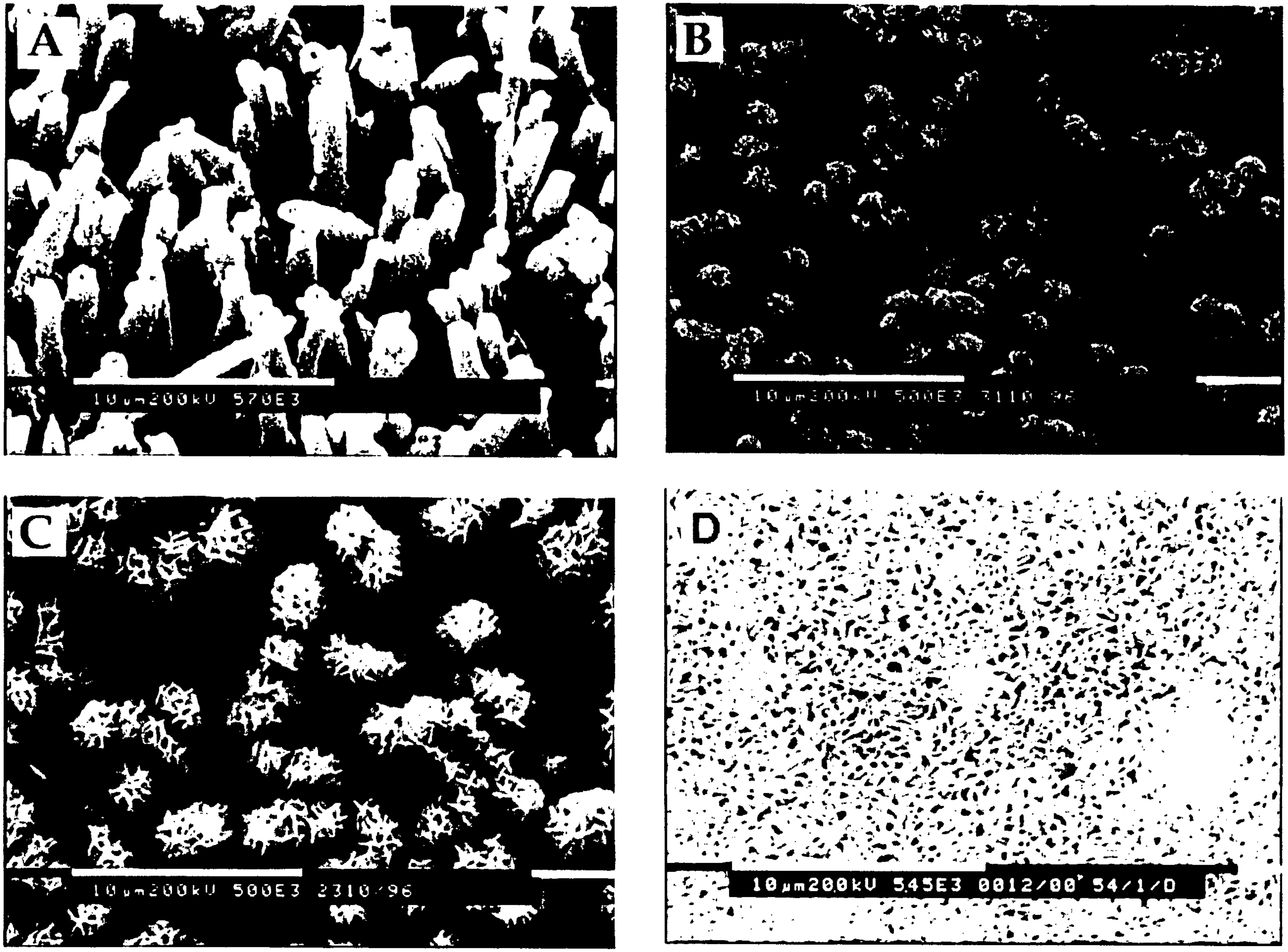
A
10μm200kU 570E3
B
10μm200kU 500E3 3110/96
C
10μm200kU 500E3 2310/96
D
10μm200kU 545E3 0012/00 54/1/D

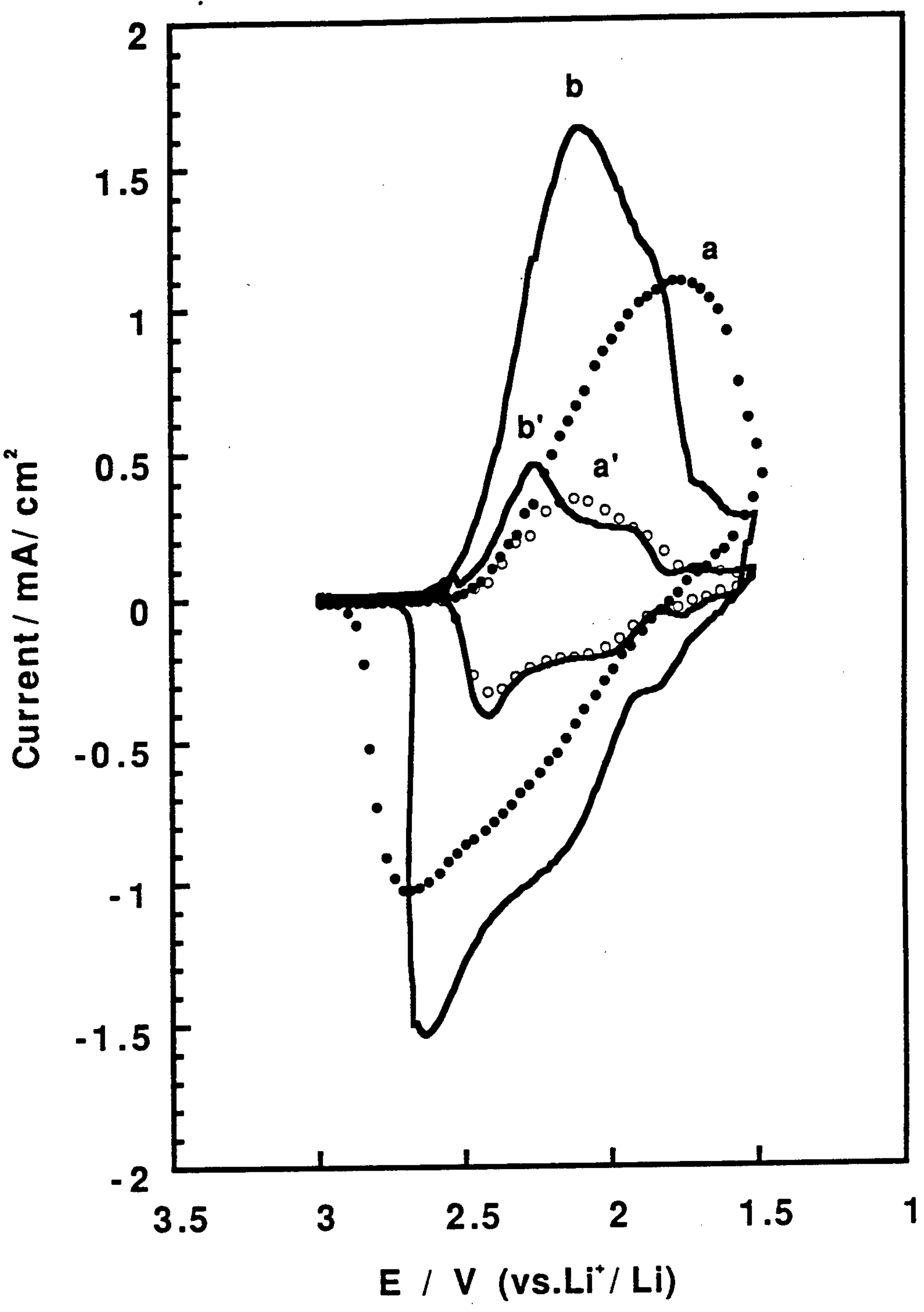
b
a
b'
a'
2
1.5
1
0.5
0
-0.5
-1
-1.5
-2
Current / mA/ cm^2
3.5
3
2.5
2
1.5
1
E / V (vs.Li$^+$/ Li)

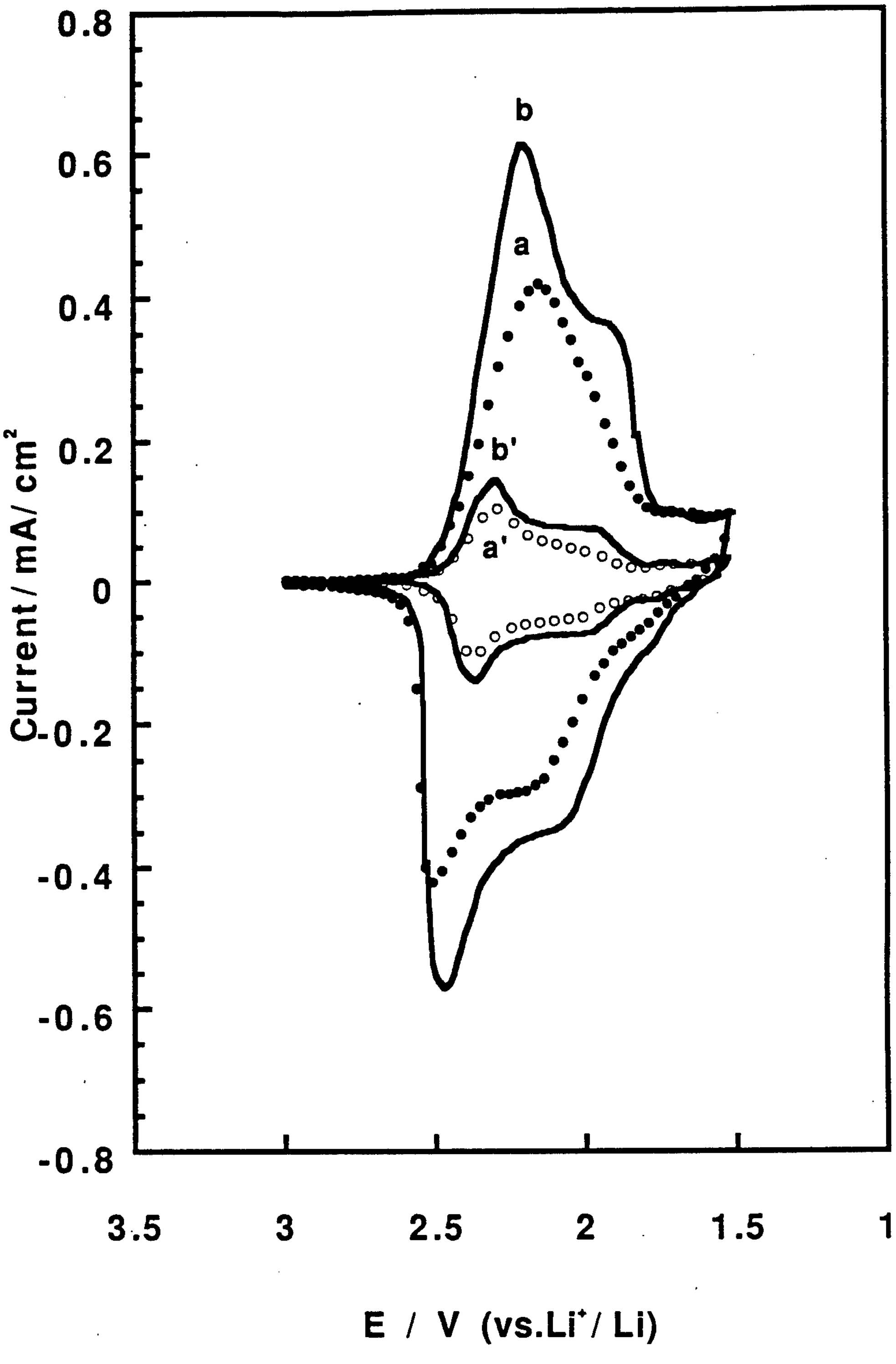

0.8
0.6
0.4
0.2
0
-0.2
-0.4
-0.6
-0.8
Current / mA/ cm^2
b
a
b'
a'
3.5
3
2.5
2
1.5
1
E / V (vs.Li$^+$/ Li)

Fig. 2

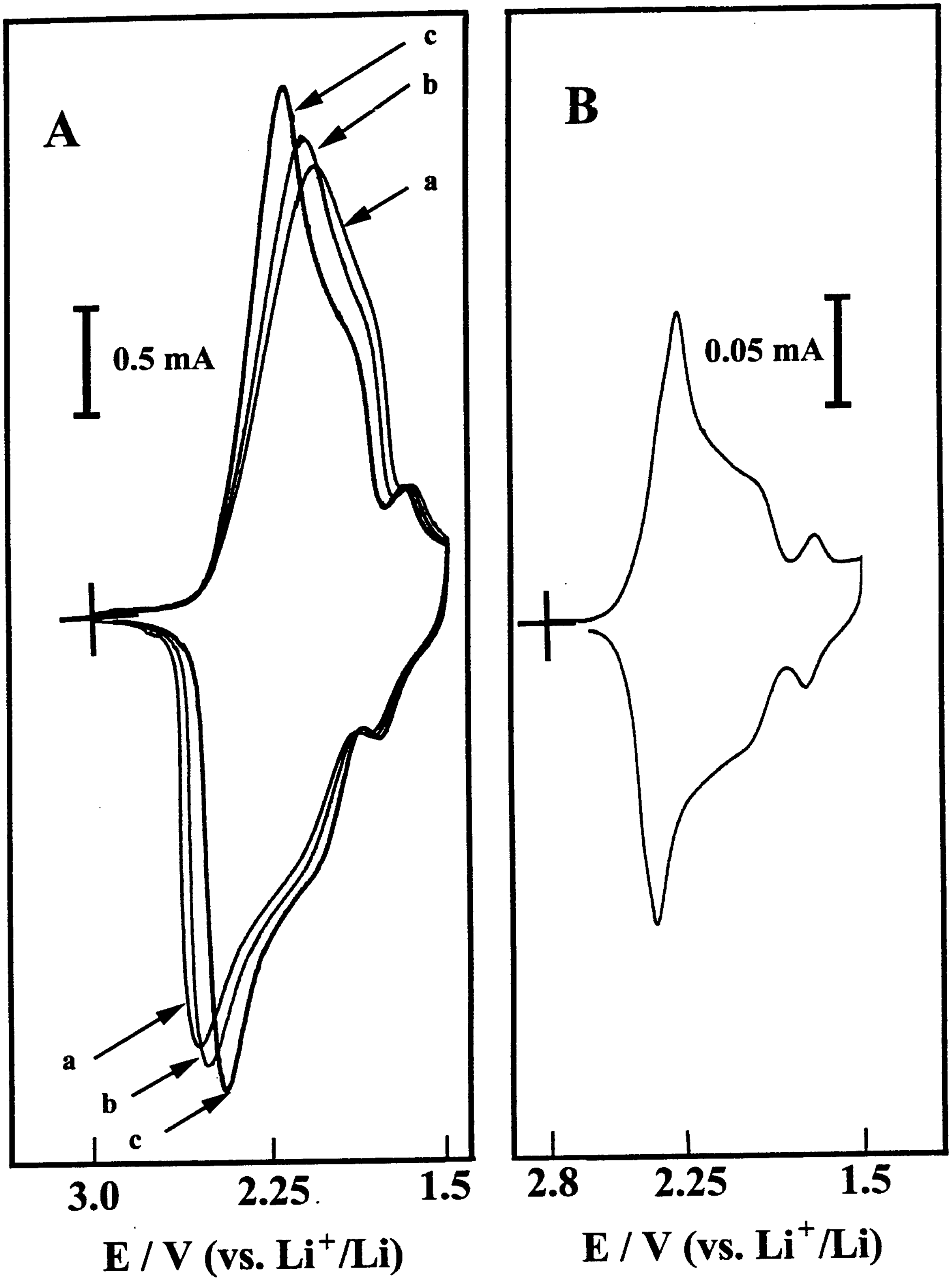

Fig 7

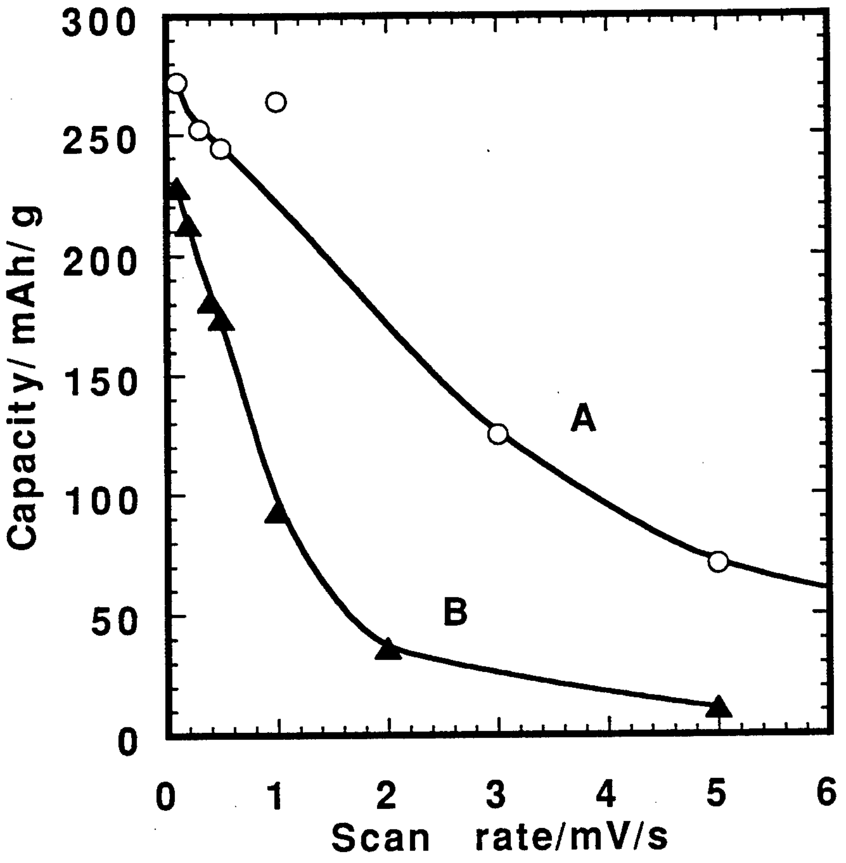
300
250
200
150
100
50
0
Capacit y/ mAh/ g
0
1
2
3
4
5
6
Scan rate/mV/s
A
B

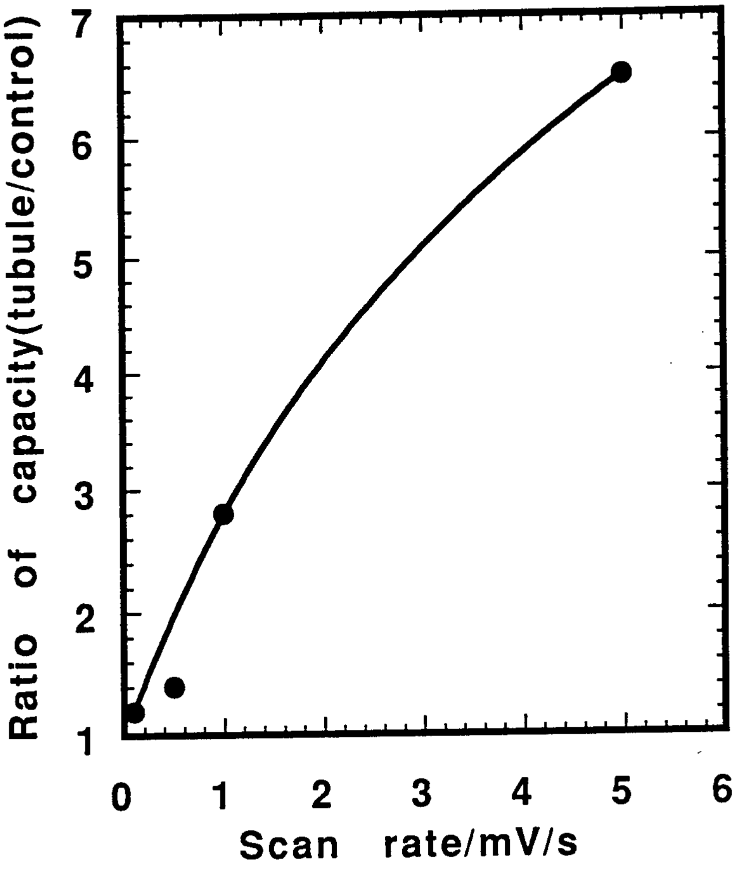
Ratio of capacity(tubule/control)
1
2
3
4
5
6
7
0
1
2
3
4
5
6
Scan rate/mV/s

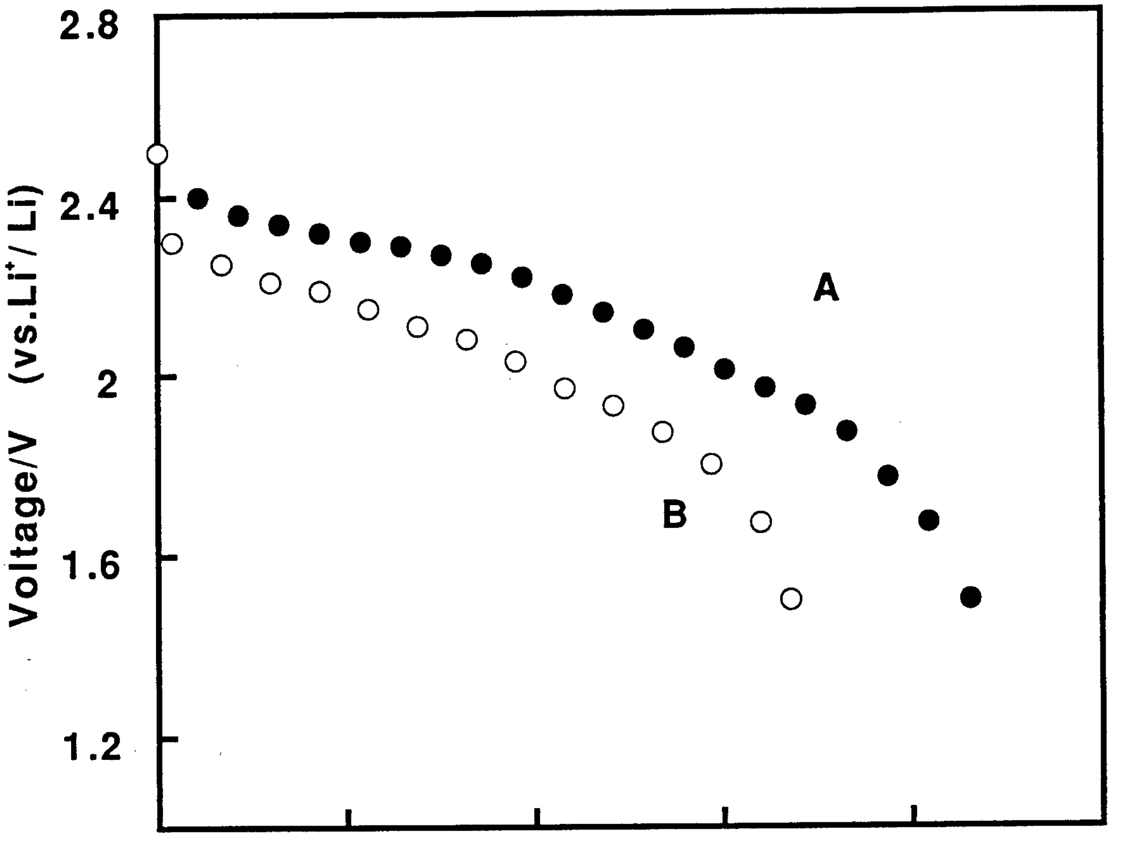
2.8
2.4
2
1.6
1.2
Voltage/V (vs.Li⁺/ Li)
0
50
100
150
200
250
Capacit y/ mAh/ g
A
B